The magmatic-hydrothermal transition record in zircon: Implications for zircon texture, composition and rare-metal granite dating (Beauvoir granite, French Massif Central).

Nicolas Esteves[1], Pierre Bouilhol[1], Urs Schaltegger[2], Maria Ovtcharova[2], André Navin Paul[2,3], Lydéric France[1,4]

[1]Université de Lorraine, CNRS, CRPG, Nancy, 54000, France
[2]Department of Earth Sciences, Université de Genève, Genève, 1200, Switzerland
[3]Institute of Geosciences, Goethe University, Frankfurt am Main, Germany
[4]Institut Universitaire de France (IUF), France

Correspondence to: Nicolas Esteves (nicolas.esteves@univ-lorraine.fr)

Abstract

Zircon petrochronology is widely used to quantify the age and duration of magma differentiation and emplacement. However, in highly differentiated magmas, such as those forming rare-metal granites, zircon may form at the magmatic-hydrothermal transition and its primary crystallisation history together with its secondary hydrothermal overprint need to be resolved and clarified. To resolve zircon formation in such an evolved and mineralised granitic system, we investigated heterogeneous zircons of the Beauvoir rare-metal granite (Massif Central, France). Most of the Beauvoir zircons are characterised by the presence of two distinct domains, designated as Zone 1 and Zone 2. Zone 1 occurs as rounded, Si- and Zr-rich domains, which are embedded in the interconnected Si- and Zr-poor Zone 2 domains that are extremely P-, U-, F-, Ca-, Fe- and Mn-rich. Both of these zones are strongly damaged (metamict) by radioactive decay, mainly from their high U concentrations. Textures and chemical composition strongly suggest that Zone 1 correspond to magmatic zircon that has been partly replaced by the Zone 2 material during the magmatic-hydrothermal transition. The crystallisation of Zone 1 zircon is preceded by the crystallisation U-rich cores (~6 wt.% UO_2) containing UO_2 (uraninite) micro-inclusions, which are then surrounded by a Zone 1 homogeneous rim. These uraninite micro-inclusions resulted from the uranium migration in the metamict and amorphous precursor zircon. Uranium-lead dating of single zircon grains using chemical abrasion, isotope dilution, thermal ionisation mass spectrometry (CA-ID-TIMS) techniques yielded a well-defined discordia line with an upper intercept at 312 ± 2.9 (7.2) Ma (2σ) and a near zero-age lower intercept. The discordancy reflects the continuous loss of radiogenic lead from a heavily damaged and aperiodic zircon lattice. On the other hand, ID-TIMS data from apatite of the Beauvoir granite yielded an age of 314.6 ± 0.1 (1.1) Ma (2σ), so far, the most accurate and precise crystallisation age of the Beauvoir granite. Thus, we emphasise that although the study of zircon from highly differentiated systems provides strong insights on the magmatic-hydrothermal transition of these objects, their metamict nature prevents their use to precisely and accurately date rare-metal granite emplacement.

1 Introduction

Peraluminous rare-metal magmatism involving highly evolved magmas is often considered to represent the ultimate stage of magmatic differentiation (e.g., Černý et al., 1985; Černý, 1992; Raimbault et al., 1995; Zoheir et al., 2020; Liu et al., 2022). This magmatism occurs either as volcanics (e.g., Pichavant et al., 1988), pegmatites (e.g., Černý et al., 1985; Van Lichtervelde et al., 2007; London, 2018) or granites (e.g., Cuney et al., 1992; Michaud et al., 2020; López-Moro et al., 2024) and is of great scientific and societal importance for being source of several critical and strategic metals (e.g., Li, Nb, Ta, Sn, W, U; see Linnen et al., 2012). The fact that these elements are mostly incompatible with respect to the main crystallising assemblage in granitic magmas, their concentrations in highly-differentiated systems (e.g., rare-metal granites, pegmatites) are governed by the various magmatic and hydrothermal processes that shape these magmatic reservoirs.

Zircon is a common mineral in granitic magmas, and it has been widely shown that it can be used to precisely monitor both the plutonic emplacement through its precise and accurate dating (e.g., Leuthold et al., 2012; Schoene et al., 2012; Barboni et al., 2013, 2015; Kryza et al., 2014; Large et al., 2020) and the subsequent magma differentiation by using its composition as a proxy (e.g., Claiborne et al., 2006; Watson et al., 2006; Schoene et al., 2012; Chelle-Michou et al., 2014; Large et al., 2020; Lu et al., 2023; Drabon et al., 2024; Farina et al., 2024). In highly differentiated, peraluminous magmatic systems, zircon often exhibits texture and composition that may be attributed to crystallisation/alteration by deuteric (i.e., melt-exsolved) fluids during the magmatic-hydrothermal transition (e.g., Černý and Siivola, 1980; Geisler et al., 2007; Schaltegger, 2007; Van Lichtervelde et al., 2009; Breiter and Škoda, 2012; Alekseev et al., 2014; Troch et al., 2018; Courtney-Davies et al., 2019; Han et al., 2023). Such zircons can be particularly rich in. Hf and U reflecting substitution reactions between zircon and its structural isomorphs (i.e., tetragonal crystal lattice). These substitution reactions respectively correspond to the hafnon ($Zr^{4+} \leftrightarrow Hf^{4+}$; Ramakrishnan et al., 1969; Speer and Cooper, 1982) and the coffinite ($Zr^{4+} \leftrightarrow U^{4+}$; Fuchs and Gebert, 1958; Förster, 2006) substitutions. Zircon can also be enriched in P, reflecting the isomorphous xenotime substitution with $Si^{4+} + Zr^{4+} \leftrightarrow P^{5+} + (REE, Sc, Y)^{3+}$ (e.g., Speer, 1980; Hoskin et al., 2000; Hanchar et al., 2001; Förster, 2006). Other elements such as Al and Ca can also incorporate zircon in addition to the xenotime substitution, corresponding to the berlinite substitution with $2Si4+ \leftrightarrow P^{5+} + Al^{3+}$ (e.g., Breiter et al., 2006; Pérez-Soba et al., 2014) and the brabantite substitution with $Si^{4+} + Zr^{4+} \leftrightarrow 2P^{5+} + Ca^{2+} + (U, Th)^{4+}$ (e.g., Pérez-Soba et al., 2014; René, 2014). The berlinite and brabantite substitutions are not isomorphous with zircon.

In addition to the lattice disordering induced by these various substitutions, the zircon structure can experience significant α-decay damage due to its U and/or Th decay, ultimately leading to a metamict and aperiodic zircon (Holland and Gottfried, 1955; Murakami et al., 1991; Nasdala et al., 1998, 2001; Geisler et al., 2003) from which the radiogenic lead (Pb*) can easily escape. Although the migration of these exotic elements is enhanced by zircon α-decay damages (Cherniak et al., 1991; Geisler et al., 2003, 2007), they can also incorporate a fresh zircon (non-metamict) directly from the melt or from hydrothermal fluids. Such early incorporation would thus provide strong constrains on melt and/or fluid composition from which zircon is crystallising (e.g., Van Lichtervelde et al., 2009; Courtney-Davies et al., 2019; Han et al., 2023), which in turn, can inform us on the processes related to mineralisation deposits.

To better understand these processes, we investigated the composition and crystal lattice of zircon from the Beauvoir rare-metal granite (Massif Central, France) through chemical and isotopic analysis and micro-Raman spectroscopy. Based on these new results, we show that primary magmatic zircon has been partially replaced during interactions with reactive hydrothermal fluids that circulated during the Beauvoir magmatic-hydrothermal transition. These replacements were accompanied with changes in zircon texture and composition, which eventually led to their amorphisation. New U-Pb age determinations by CA-ID-TIMS (chemical-abrasion isotope-dilution thermal ionisation mass spectrometry) reflect the advanced state of lattice damage and continuous loss of radiogenic Pb, yielding to strongly discordant data with an upper intercept at 312 ± 7.2 Ma (2σ). Although our data from zircon of Beauvoir rare-metal granite provides strong insights on the Beauvoir magmatic-hydrothermal transition, we demonstrate that ID-TIMS U-Pb geochronology of apatite can yield to accurate estimation of rare-metal granite emplacement dating, which correspond to 314.6 ± 0.1 (1.1) Ma for the Beauvoir intrusion.

2 The Beauvoir granite

2.1 Geological setting

The Beauvoir rare-metal granite is located in the Sioule area (

Figure 1), which corresponds to an inverted metamorphic sequence (Grolier, 1971) in the northern part of the Variscan Massif Central (France). The Sioule area is bordered by two major fault systems, the late Carboniferous Sillon Houiller to the west and the Oligocene Ebreuil graben to the east. From top to bottom, this metamorphic series is composed by a cordierite migmatite overlying a biotite-sillimanite gneiss, referred to the Upper-Gneiss Unit (UGU; Grolier, 1971; Faure et al., 1993). A two-micas paragneiss is located structurally below the UGU and corresponds to the Lower-Gneiss Unit (LGU), whereas a staurolite-bearing micaschist is located at the base of this metamorphic series (

Figure 1; Grolier, 1971; Faure et al., 1993). This micaschist corresponds to the Para-Autochthonous Unit. The whole series experienced a Barrovian-type metamorphism at ca. 365-350 Ma (Do Couto et al., 2016) that has been linked to the collision between Armorica and the Avalonia-Laurentia block following the closure of the Rheic Ocean (Faure et al., 2009).

The Beauvoir rare-metal granite together with the Colettes leucogranite forms the Echassières granitic complex (

Figure 1)). Their intrusions into the micaschist series produced a contact aureole overprinting the regional metamorphic assemblages (Merceron et al., 1992). The Colettes leucogranite represents the main body of the Echassières complex and was emplaced at 317 ± 8 Ma (Rb-Sr whole rock from Pin, 1991 recalculated by Carr et al., 2021). The Beauvoir rare-metal granite is thought to have subsequently intruded to the Colettes leucogranite as the latter is affected by a metasomatic aureole at the contact with the Beauvoir intrusion (Aubert, 1969; Raimbault et al., 1995). Detailed studies on the Beauvoir granite fluids inclusions document an emplacement pressure of 80 MPa, corresponding to an emplacement depth of ~3 km (Aïssa et al., 1987; Cuney et al., 1992).

Several studies attempted to date the Beauvoir granite crystallisation using various minerals and approaches. An age of 308 ± 2 Ma have been proposed by Cheilletz et al. (1992) by using ^{40}Ar-^{39}Ar dating on lepidolite whereas Melleton et al. (2015) estimated 317 ± 6 Ma via U-Pb on columbite-tantalite. These datings are consistent with the new Beauvoir apatite age proposed by Rocher et al. (2024) at 314.6 ± 4.7 Ma (U-Pb; LA-ICP MS). A third magma body (La Bosse), inferred to be the source of the wolframite-bearing La Bosse stockwork (

Figure 2), has been dated by Carr et al. (2021) at 316.7 ± 3.3 Ma (U-Pb on wolframite). The Sioule metamorphic series also host other Variscan granitoids such as the Pouzol-Servant microgranite (ca. 330 Ma; Pin, 1991;

Figure 1), the Chantelle granite, the Champs granite as well as late Visean volcanic deposits (ca. 330 Ma; Do Couto et al., 2016).

2.2 The Beauvoir rare-metal granite

The Beauvoir intrusion (

Figure 2) consists of a leucocratic rare-metal granite. Its mineral assemblage is composed of quartz, albite, K-feldspar, lepidolite (Li-mica), topaz and amblygonite (Li-phosphate). Accessory minerals disseminated across the granite are in order of abundance: F-apatite, cassiterite (SnO_2), columbite-tantalite (Mn-Fe, Nb-Ta_2O_6), zircon, microlite (Na-Ca_2-U, Ta_2O_6) and uraninite (UO_2). From bottom to top, the Beauvoir intrusion is characterised by an increase of incompatible element contents (e.g., Be, Li, P, F, Rb or Ta) and an overall decrease in compatible element contents (e.g., Fe, Mn, Ti or Zn). Variations of these elements are associated with a global increase of the Rb/K and the Hf/Zr ratios, that are consistent with increasing magma differentiation toward the top of the pluton (Raimbault et al., 1995; Rossi et al., 1987). Based on bulk-rock chemistry, Gagny (1987) showed that the Beauvoir intrusion resulted of the stacking of numerous magmatic batches.

A similar conclusion has been recently drawn by Esteves et al. (2024), who showed that the Beauvoir intrusion was built through the stacking of at least eighteen crystal-poor sills (i.e., sub-units in

Figure 2). Based on systematic changes in sill lepidolite composition, the authors showed that each of these sills represents residual magma that was episodically extracted from a deeper differentiating reservoir. Such deep differentiation processes would have occurred four times, corresponding to the four Beauvoir units (U_1 to U_4 in

Figure 2; Esteves et al., 2024). Once injected, the progressive crystallisation of these sills has led to the formation of Na-, Al-, Li-, P-, and F-rich residual melts that percolated in channels through the granitic mush before its entire solidification. From melting and crystallisation experiments using Beauvoir samples as starting materials, Pichavant (2022) estimated a solidus temperature around 550 °C. Such low solidus temperature can be explained by the high volatile and Li content that strongly reduce magma solidus temperature (Wyllie and Tuttle, 1964; London, 1992; Scaillet et al., 1995). Concomitantly to crystallisation of Beauvoir magmas, a hydrothermal activity has taken place involving several different aqueous fluids and chorine-rich brines stages (Aïssa et al., 1987; Fouillac et al., 1987; Harlaux et al., 2017; Rocher et al., 2024).

Zircon grains in the Beauvoir granite (size ~20-80 µm) crystallised as octahedral crystals displaying a perfect bi-pyramidal shape (Figure 3a-f). A second acicular group have been locally observed in the Beauvoir unit 1 and 2. Zircons are commonly enclosed in lepidolite and caused pleochroic halos in host minerals. Those zircons are Hf-rich (up to 19.15 wt.% HfO_2)

reflecting the zircon-hafnon substitution (Breiter and Škoda, 2012) and U-rich (up to 9.69 wt.% UO_2) due to the zircon-coffinite substitution (Breiter and Škoda, 2012). Although Breiter and Škoda (2012) analysed 31 oxides including rare-earth-elements (REE), their analytical oxide sums ranged from ~92 to 100%, and thus proposed that water might be present in these zircon. Although metamict crystals have been ubiquitously identified across the granite, potential zircon crystals with a lower degree of decay damage were optically identified at various depths by Rossi et al. (1987).

Three distinct apatite generations have been recognised in the Beauvoir intrusion (Rocher et al., 2024), all of them corresponding to fluoro-apatite. The first generation (Apatite I) refers to early and magmatic apatite. These grains (up to 0.5 mm) are often included in or in close relation with topaz crystals and are easily recognised with bluish colour in natural light. This magmatic generation is characterised by a high amount of manganese (up to 6.5 wt.% MnO; Rocher et al., 2024), which can enter the calcium site. The incorporation of Mn is expected to explain its bluish colour (Ribeiro et al., 2005). The second and third apatite generations (Apatite II and III) crystallised during the early and late Beauvoir hydrothermal circulation events, respectively (Rocher et al., 2024). They are colourless in natural light and are depleted in manganese compared to the first generation (Cuney and Autran, 1988; Rocher et al., 2024).

3 Material and methods

Samples were collected from the 900 m GPF-1 borehole stored at the Bureau de Recherches Géologiques et Minières (BRGM; Orléans, France). Sampling was conducted at specific depths, where Rossi et al. (1987) had observed the presence of "fresh" zircons (i.e., weakly damaged), leading to a total of twelve samples (

Figure 2). Samples are labelled by "GPF-depth" (for instance GPF-352.30 was collected at a depth of 352.3 m). Rock samples fragmentation was performed by using the Selfrag Lab apparatus (i.e., high-voltage pulse fragmentation technology from SELFRAG AG, Switzerland) installed at the GeoRessources laboratory (Steval platform, Vandoeuvre-lès-Nancy, France). To efficiently allows crystal liberation along grain boundaries, this fragmentation was done under 120 kV, a pulse rate of 5 Hz for a total of ~100 pulses. Heavy fractions of these obtained sands, in which zircon and apatite are concentrated (along with topaz, cassiterite, columbite-tantalite and microlite), were then separated from the rock light fractions (i.e., quartz, feldspar and mica) by using both a shaking table at the Centre de Recherches Pétrographiques et Géochimique (CRPG; Vandoeuvre-lès-Nancy, France) and subsequent heavy liquids (diiodomethane, density 3.32) at the Department of Earth Sciences at the University of Geneva (Switzerland). Zircon and bluish apatite were then handpicked under binocular microscope. Zircon crystals from GPF-680.60 and GPF-598.05 (

Figure 2) were mounted in epoxy resin for micro-Raman and electron-probe analyses.

3.1 Imaging, micro-Raman and composition analyses of zircon

The backscattered electron (BSE) images were obtained using a JEOL JXA 8230 microprobe at the CRPG under 15 kV and 15 nA. Micro-Raman measurements were performed using a high-resolution LabRAM (Jobin-Yvon®, Horiba) at GeoRessources (Nancy, France) coupled to a 50× optical microscope (Olympus®). Zircon spectra were obtained using a neon laser (515 nm) with a laser power of 300 mW, resulting in an energy of 30 mW at the surface sample. Slit width was 200 µm. The energy band of neon glow lamps was used for calibration. To evaluate the ν_3 (SiO_4) zircon Raman internal vibration mode, spectra were collected in the spectral interval between 843 and 1250 cm^{-1} with a spectral resolution of 2.5 cm^{-1}. Extended zircon Raman spectra were also collected between 100 and 1200 cm^{-1}. The other internal modes (ν_1, ν_2 and ν_4) that are related to Si and O vibrations within the SiO_4 tetrahedron (Dawson et al., 1971) were not analysed due to their low intensity. A spot size of 1 µm and a dwell time of 0.1 s was used to collect the micro-Raman maps whereas individual micro-Raman analyses were measured with an acquisition time of 1 s, accumulated ten times. All measurements were performed in one session. All spectra were baseline corrected using the Labspec® software, from which the peak position and peak linewidth were calculated. Linewidth was then corrected following the equation given by Tanabe and Hiraishi (1980), providing the real FWHM (full width at half maximum) of the Raman peak:

$$\Gamma = \Gamma_m \left[1 - \left(\frac{S}{\Gamma_m}\right)^2\right]$$

where Γ is the corrected linewidth, Γ_m is the measured linewidth from Labspec software and S the spectral resolution.

Following the micro-Raman measurements, both point analyses and chemical maps have been performed on an electron probe using a CAMECA SXFIVE-Tactis at the GeoRessources laboratory (Vandoeuvre-lès-Nancy, France). Each point analyses have been conducted under 10 nA current and 15 kV accelerating voltage with a 1 µm-diameter focused beam. Eleven element oxides were calibrated using zircon (Si, Zr), corundum (Al), $MnTiO_3$ (Mn), Fe_2O_3 (Fe), wollastonite (Ca), apatite (P), topaz (F), metallic Hf (Hf), thorium (Th) and uraninite (U). Counting times were 10 s on the peak and 5 s on the background for each element. Chemical X-ray maps were performed under 40 nA current, a 15 kV accelerating voltage, a 50 ms of dwell time with a pixel size of 0.25 µm. X-ray maps were cross-calibrated with quantitative point analyses to obtain quantitative X-ray maps by using XMapTools 4.2 (Lanari et al., 2014, 2019). Although the investigated zircon grains are coming from distinct samples, they will be treated together as their compositional analyses are overlapping. The various dark inclusions in zircon (Figure 3a-f) have been identified and analysed using a JEOL 6510 SEM (scanning electron microscope) at the Centre de Recherches Pétrographiques et Géochimiques (Vandoeuvre-lès-Nancy, France).

From the U and Th concentration, the α-fluence (D_α) corresponding to the number of emitted α-particles per mg of each analysed zircon was calculated following the equation of Nasdala et al. (2001):

$$D_\alpha = 8 \times \frac{C_U \times N_A \times 0.9928}{M_{238} \times 10^9}\left(e^{\lambda^{238}t} - 1\right) + 7 \times \frac{C_U \times N_A \times 0.0072}{M_{235} \times 10^9}\left(e^{\lambda^{235}t} - 1\right) + 6 \times \frac{C_{Th} \times N_A}{M_{232} \times 10^9}\left(e^{\lambda^{232}t} - 1\right)$$

where C_U and C_{Th} correspond to the U and Th concentration in µg/g, N_A is the Avogadro constant ($6.022.10^{23}$), M_{238}, M_{235} and M_{232} are respectively the molecular weight of ^{238}U, ^{235}U ^{232}Th. λ^{238}, λ^{235} and λ^{232} are their respective decay constant from Jaffey et al. (1971) and Le Roux and Glendenin (1963). t is the zircon crystallisation age, here 314.6 Ma (see below).

Table 1. Representative chemical composition and structural formula of the Beauvoir zircons. Structural formulas are calculated on the basis of two cations and four oxygens. Elements that are enriched in Zone 2 compared to Zone 1 are in bold. See the supplementary materials S1 for the whole data set and the supplementary figure S1 for the localisation of each analysis. 0.0 analyses are below the detection limit.

	Zone 1 (n = 51)				Zone 2 (n = 37)				Detection limits (D.L)
	Mean	Max	Min	SD	Mean	Max	Min	SD	wt.%
SiO_2 (wt.%)	30.41	32.86	25.58	1.69	23.23	31.58	16.56	4.43	0.13
Al_2O_3	0.16	1.61	0.00	0.27	1.25	2.69	0.00	0.68	0.11
FeO	0.22	1.72	0.00	0.40	0.78	2.10	0.00	0.57	0.13
MnO	0.08	0.47	0.00	0.10	0.47	1.08	0.00	0.26	0.13
CaO	0.20	1.26	0.00	0.26	1.73	3.69	0.00	1.04	0.06
P_2O_5	0.40	1.83	0.00	0.42	3.69	10.06	0.11	3.13	0.33
ZrO_2	61.68	65.83	51.48	2.61	51.98	64.84	39.05	5.80	0.25
HfO_2	4.30	9.99	2.63	1.45	3.10	6.45	2.04	0.79	0.45
ThO_2	0.02	0.13	0.00	0.04	0.02	0.17	0.00	0.04	0.22
UO_2	0.97	5.44	0.09	1.19	3.31	7.80	0.45	1.93	0.25
F	0.40	1.51	0.00	0.39	1.81	3.58	0.19	0.91	0.73
Total	98.84				91.36				
α-doses (10^{16}/mg)	0.85				2.95				
Number of ions on the basis of four oxygens									
Four-coordinated cations (T-site)									
Si (apfu)	0.96	1.01	0.85	0.04	0.78	0.98	0.54	0.13	
Al	0.01	0.06	0.00	0.01	0.05	0.11	0.00	0.03	
P	0.01	0.05	0.00	0.01	0.11	0.29	0.00	0.09	
Sum	0.98				0.94				
Eight-coordinated cations (A-site)									
Fe (apfu)	0.01	0.05	0.00	0.01	0.02	0.06	0.00	0.02	
Mn	0.00	0.01	0.00	0.00	0.01	0.03	0.00	0.01	
Ca	0.01	0.05	0.00	0.01	0.06	0.13	0.00	0.04	
Zr	0.95	1.00	0.86	0.03	0.85	0.98	0.68	0.07	
Hf	0.04	0.09	0.02	0.01	0.03	0.07	0.02	0.01	
Th	0.00	0.00	0.00	0.00	0.00	0.00	0.00	0.00	
U	0.01	0.04	0.00	0.01	0.03	0.06	0.00	0.02	
Sum	1.01				1.00				
Anionic site									
F	0.04	0.16	0.00	0.04	0.19	0.37	0.02	0.10	

3.2 U-Pb dating of zircon and apatite

Zircon and apatite U-Pb geochronology was conducted in the Department of Earth Sciences at the University of Geneva (Switzerland). Hand-picked zircon crystals separated for geochronological analyses were first annealed at 900 °C during 48 hours in an oven. This annealing step allows zircon to partially recover their crystallographic structures. The annealed zircons then underwent a first washing step using ethanol before being washed a second and a third time with a 7 N HNO_3 solution with a sonic bath. Each grain was placed in Savillex microcapsules along with four drops of concentrated HF. These microcapsules were placed in a Parr bomb vessel at 210 °C for 3 h. The objective of this partial dissolution step is to dissolve the more strongly decay-damaged zones in the zircon which are also likely to contain elevated contents of common lead (Pb_c). Although the optimal duration of this partial dissolution step is estimated to be 8-12 h (Widmann et al., 2019; McKanna et al., 2024) , our zircons were already completely dissolved after 3 h. Solutions of the sample GPF-598.05 (i.e. corresponding to fully dissolved zircon) were dried before being spiked with one drop of the EARTHTIME ^{202}Pb-^{205}Pb-^{233}U-^{235}U tracer solution together with three drops of 6 N HCl. With this knowledge that the Beauvoir zircons might not survive to the partial dissolution step, zircons from further samples GPF-352.30, 447.60, 784.73, 824.20 and 860.25 were spiked before the dissolution step using the EARTHTIME ^{205}Pb-^{233}U-^{235}U tracer solution. These solutions were also dried before three drops of 6 N HCl were added to their respective microcapsules. All samples were dried again and redissolved in three drops of 3.1 N HCl. Uranium and lead elution were isolated via an anion exchange resin using HCl and H_2O. One drop of H_3PO_4 was added to the elution solution before evaporation on a hot plate.

Apatite was analysed as individual crystals or fragments, having variable size ranging from ~50 µm to ~200 µm. Individual fragments were washed in 3 ml Savillex beakers in an ultrasonic bath (four times, using de-ionised ultrapure water). The fragments were then transferred into individual 200 µL Savillex microcapsules, along with 2-3 drops of 6 N HCl and 4.8 to 17.8 mg of a mixed ^{205}Pb-^{233}U-^{235}U tracer solution (ET535; Condon et al., 2015; McLean et al., 2015), and completely dissolved at 210 °C in a Parr bomb vessel for 24 h. After dissolution, samples were dried down on a hot plate at 120 °C, re-dissolved in 1 M HBr, and then U and Pb were separated using a modified HBr based single column anion exchange chemistry (Paul et al., 2021).

U and Pb for zircon and apatite chemistry were loaded separately on outgassed, zone-refined, single Re filaments with a silica-gel/phosphoric acid emitter solution, modified after Gerstenberger and Haase (1997). The U and Pb isotopic compositions were measured on an Isotopx Phoenix TIMS (thermal ionisation mass spectrometer) at the Radiogenic Isotopes Laboratory, University of Geneva. Electronic baselines and ATONA calibration were conducted for 12 h each at the beginning of the analytical work. U was measured in static mode using ATONA amplifiers, with U analysed as an oxide. Pb was analysed in a mixed Faraday-Daly configuration, with ^{204}Pb measured on the Daly, in a one jump setup (real time correction, ^{204}Pb and ^{205}Pb on Daly) or in peak jumping mode using only Daly detection. Measured isotopic ratios were corrected for interferences of $^{238}U^{18}O^{16}O$ on $^{235}U^{16}O_2$ using a $^{18}O/^{16}O$ composition of 0.00205, based on repeat measurements of the U500 standard. Mass fractionation of U was corrected using a double isotope tracer with a $^{235}U/^{233}U$ of 0.99506 ± 0.005. Mass fractionation of Pb was corrected using repeat analyses of SRM 981 standard ($\alpha = 0.20 \pm 0.02$ %/a.m.u .± 1σ abs.). Apatite Pb analyses were corrected for laboratory blanks, which were estimated to be 0.84 ± 0.23 pg, with a $^{206}Pb/^{204}Pb$ of 18.50 ± 0.74, a $^{207}Pb/^{204}Pb$ of 15.58 ± 0.31 and a $^{208}Pb/^{204}Pb$ of 38.17 ± 1.14, based on repeat measurements (n = 14) of total procedural blanks for HBr column chemistry. Initial Pb in apatite was corrected using a ^{204}Pb based correction, using a model initial Pb isotopic composition equivalent to the Stacey and Kramers (1975) two-stage model Pb-growth curve at 300 Ma. All data were processed using the Tripoli, YourLab and Isoplot software/excel packages (Ludwig, 1991; Bowring et al., 2011; McLean et al., 2011; Schmitz and Schoene, 2007). Thorium abundances for each apatite grain, and subsequently $Th/U_{apatite}$, were calculated using the abundance of ^{208}Pb within the crystal and the $^{206}Pb/^{238}U$ age to calculate radiogenic in-growth (McLean et al., 2011). Zircon and apatite U-Pb age uncertainties were obtained using Isotplot software (Ludwig, 1998) and are reported at the 2 σ level in the format $A \pm X$ (Y), where A corresponds to the estimated age, X is analytical uncertainty associated to A and Y is the analytical uncertainty combined with the data overdispersion (i.e., MSWD).

4 Results

4.1 Zircon texture

Under BSE imaging, the Beauvoir zircons exhibit heterogeneous textures consisting of bright and dark materials (i.e., contrasting composition), respectively identified as zircon Zone 1 and 2 (Figure 3a-c). Zircon inner parts present a mixture of small rounded-like pieces (up to 5 µm) of Zone 1 material embedded in the interconnected, braided Zone 2 material (Figure 3a-c). Around these cores, zircons alternate between homogeneous dark material (Zone 2) and Zone 1 growth zones (e.g., Figure 3c). Zone 1 growth zones contain abundant cracks (< 1 µm) that are filled by Zone 2 material. Zircon outer rims are similar to the core with the presence of rounded Zone 1 material within Zone 2 matrix. Beauvoir zircons also contain numerous muscovite and quartz inclusions (Table S1 and Figure S2) that appear black in BSE images (e.g., Figure 3b, c). These inclusions are locally connected to cracks (Figure 3d). Columbite-tantalite is also present in one of these dark inclusions (Figure 3e). Another zircon population represented by Zr-5 (Figure 3f) displays a core containing numerous uraninite micro-inclusions (size ~1-2 µm). The transition from core to rim is sharp as these uraninite inclusions are absent in this zircon rim. BSE intensity indicates that Zr-5 rim is composed of a denser material than the one in the core. Zircons with typical oscillatory zoning or inherited cores are absent in our sample set.

4.2 Zircon electron-probe and micro-Raman analyses

Representative compositions of the Beauvoir zircons are documented in **Erreur ! Source du renvoi introuvable.**, and compositional variations between Zone 1 and 2 are represented in the various diagrams of Figure 4a-h. Compositional variations of Zr-3 and Zr-1 are compared to their BSE images in Figure 5a-f and Figure 6a-f, respectively. From Zone 1 & 2 composition, several types of ionic substitution can be identified allowing the incorporation of various elements in these zircons.

1. “**Berlinite**” substitution [2 $Si^{4+} \leftrightarrow P^{5+} + Al^{3+}$]: Zone 1 corresponding to the bright material in BSE images is enriched in Si compared to Zone 2 with an average of 30.41 and 23.23 wt.% SiO_2, respectively (Figure 4a, Figure 5a, b and Figure 6a, b). Cracks are also depleted in Si. For comparison, pure zircon (i.e., $ZrSiO_4$) has 32.8 wt.% SiO_2 (Hoskin and Schaltegger, 2003). Si in Zone 1 zircon T-site decreases to 0.85 (i.e., 25.58 wt.% SiO_2) and to 0.54 apfu Si (i.e., 16.56 wt.% SiO_2) in Zone 2 (Figure 4a; **Erreur ! Source du renvoi introuvable.**). Si negatively correlates with P + Al (Figure 4a), and forms a linear trend slightly below the berlinite substitution vector. This substitution is clearly visible in the chemical maps where Si-rich materials (Zone 1) are depleted in P and vice versa (Figure 5b, f and Figure 6b, f). The extent of berlinite substitution is limited in Zone 1 compared to Zone 2, leading to a Zone 1 T-site almost exclusively filled with Si while up to 0.05 apfu Al (1.25 wt.% Al_2O_3) and 0.11 apfu P (3.69 wt.% P_2O_5) enter the Zone 2 T-site. As the berlinite substitution involves the incorporation of one P^{5+} and Al^{3+} instead of 2 Si^{4+}, the enrichment in P over Al in the Beauvoir zircons (Figure 4b) implies that P^{5+} was also incorporated by another substitution.

2. “**Brabantite**” substitution [2 Si^{4+} + 2 $Zr^{4+} \leftrightarrow Ca^{2+} + (U^{4+}) + 2P^{5+}$]: Ca in Beauvoir zircon negatively correlates with Si, forming a linear trend below the brabantite substitution vector (Figure 4c). On average, Ca is enriched in Zone 2 compared to Zone 1 (1.73 vs 0.20 wt.% CaO, respectively; **Erreur ! Source du renvoi introuvable.**). Zircon data are slightly above the brabantite substituting vector when Ca is against P*, where P* = P-Al (apfu) represents the extra P^{5+} that need to be charge-balanced after the berlinite substitution (Figure 4d).

3. **Incorporation of F**: Zone 2 is particularly rich in F (Figure 4e) with an average composition of 1.81 wt.% F and a maximum of 3.58 wt.% F (0.37 apfu F) whereas it is poorer in Zone 1 (mean of 0.4 wt.% F where most of the analyses are below the detection limit; **Erreur ! Source du renvoi introuvable.**). F negatively correlates with Si forming a linear trend with a 1:1 slope in this chemical space (Figure 4e).

4. **Hafnon** substitution: Zr, which is the main constituent in zircon is enriched in Zone 1 (Figure 4f-h, Figure 5c and Figure 6c) with an average concentration of 61.68 wt.% ZrO_2 compared to Zone 2 (51.98 wt.% ZrO_2; Table 1). Such concentrations correspond to a Zone 1 A-site on averaged filled by 0.95 and 0.85 apfu Zr in Zone 2. Although Hf does not correlate with Zr (Figure 4f), the highest Hf concentration has been found in Zone 1 (9.99 wt.% HfO_2; **Erreur ! Source du renvoi introuvable.**). From the chemical maps, Hf-rich areas (indicated by an arrow in Figure 6d) are also enriched in Si and Zr.

5. **Incorporation of U:** U negatively correlates with Zr (**Figure 4**g) and is, on average depleted in Zone 1 compared to Zone 2 (0.97 vs 3.31 wt.% UO_2; **Erreur ! Source du renvoi introuvable.)**. The U-Zr covariation is well below the coffinite substitution vector ($Zr^{4+} \leftrightarrow U^{4+}$, **Figure 4**g). U strongly correlates with P (**Figure 5**e, f and **Figure 6**e, f) whereas it it also

negatively correlates with Si (**Figure 5**b, c, e and **Figure 6**b, c, e). Th concentration in Beauvoir zircon is generally below the detection limits **(Erreur ! Source du renvoi introuvable.)**.

6. **Incorporation of low-field strength cations Mn and Fe**: Unusual elements for a zircon such as Fe and Mn are enriched in Zone 2 (0.78 wt.% FeO and 0.47 wt.% MnO, respectively) compared to Zone 1 where most of the analyses are below the detection limits (**Erreur ! Source du renvoi introuvable.**). For zircon containing more than 0.90 apfu Zr , Mn + Fe negatively correlates with Zr in agreement with the theoretical $Zr^{4+} \leftrightarrow Mn^{2+} + Fe^{2+}$ substitution vector (Figure 4h). For a Zr below 0.90 apfu, Mn + Fe does not correlate with Zr (Figure 4h). The oxide sum are on average 98.84 in Zone 1, while it is 91.36 wt.% in Zone 2 (**Erreur ! Source du renvoi introuvable.**). The calculated structural formulas highlight that this low total in Zone 2 corresponds to a cation deficiency in the T-site (0.94 instead of 1 apfu) whereas the A-site is fully occupied in both Zone 1 and 2. Such low oxide sum in Beauvoir Zone 2 indicates the non-dosage of various elements (such as H_2O). Zr-5 displayed in Figure 3f is texturally different from the other Beauvoir zircons but is compositionally similar to the Zone 1. These results are consistent with the previously published Beauvoir zircons analyses by Cuney & Autran (1988) and Breiter & Škoda (2012).

Among these substitutions, the zircon-hafnon and zircon-coffinite substitutions represent the chemical evolution between two end-member of a solid solution as they are all tetragonal (i.e., zircon, hafnon and coffinite share the same crystal structure) whereas the berlinite and brabantite substitution do not represent isomorphous substitutions with zircon.

The comparison between the Zr-1 micro-Raman signature of Zone 1 and 2 with its chemical maps is presented in Figure 6a-i. Although the Raman intensity is rarely used as a discriminating parameter in Raman spectroscopy (i.e., the intensity is often labelled in arbitrary unit), it strongly correlates with zircon SiO_2 and ZrO_2 concentrations (Figure 6b, c and g) and can thus be used to identified Zone 1 zircon. In other words, the Raman intensity decrease is correlated to the substitutional degree of the analysed material. The ν_3 (SiO_4) linewidth of Zr-1 is negatively correlated with its ν_3 (SiO_4) intensity (Figure 6g, h) as well as with SiO_2, ZrO_2 and HfO_2. On the other hand, it correlates with UO_2 and P_2O_5 concentrations, leading to a lower ν_3 (SiO_4) linewidth for Zone 1 compared to Zone 2 (~15 to 25 vs 30 to 40, respectively, Figure 6h). The Beauvoir zircons ν_3 (SiO_4) linewidth negatively correlates with their ν_3 (SiO_4) peak position (Figure 7a). Analyses leading to ν_3 (SiO_4) linewidth below 25 cm^{-1} are exclusively referring to Zone 1 whereas an overlap exists between Zone 1 and Zone 2 above 25 cm^{-1} (Figure 7a). Although their ν_3 (SiO_4) linewidth correlates, in the first order, with the α-decays/mg they experienced, two trends can be distinguished on the diagram (Figure 7b). Indeed, the slope of these trends significantly differs from Zone 1 to Zone 2, with a weaker one for Zone 1 (Figure 7b). Thus, although Zone 1 and 2 can have a similar ν_3 (SiO_4) linewidth, the α-decays/mg that experienced Zone 2 is two to six times higher than what experienced Zone 1 (Figure 7b). Typical extended Beauvoir zircon Raman spectra are displayed on Figure 7c and can be compared to the spectrum of a non-damaged zircon (RRUFF database; Lafuente et al., 2015). Zircon spectra with the weaker ν_3 (SiO_4) linewidth are those where the zircon Raman bands are the best expressed (e.g., little disordered Zone 1; Figure 7c). On the other hand, ν_1 and ν_3 (SiO_4) cannot be distinguished on Zone 2 metamict zircon spectrum (Figure 7c). During this study, any micro-Raman analyses yielded to very well-ordered zircon with a ν_3 (SiO_4) linewidth below 10 cm^{-1}.

4.3 Zircon and apatite geochronology

All analysed Beauvoir zircons are discordant and contain variable amount of common lead (0.74 to 82.8 pg; Table S1). Analyses with a high uncertainty (i.e., large ellipse in Figure 8a) are those with a high Pb_c/Pb^* ratio (greater than 1) whereas more precise analyses are those with smaller ellipses and low Pb_c/Pb^* ratio. Therefore, although the Beauvoir granite is composed of several magmatic batches (
Figure 2; e.g., Gagny, 1987), all analysed zircons have been grouped together because the precision of each discordia regression line does not allow us to distinguish different magma batches. Despite their discordant nature, all zircons (except one grain) are aligned along a single Discordia line, which indicates an upper intercept age of 312.0 ± 2.9 (7.2) Ma (2σ). The lower intercept of the discordia line is near the zero-age at 4.1 ± 1.4 (3.7) Ma (Figure 8a). Of the 37 grains analysed, none provided an age older than the expected Variscan age of the Beauvoir granite.

Uranium-lead analyses of apatite yielded concordant $^{206}Pb/^{238}U$ ages, after initial Pb correction using a Stacey and Kramers (1975) two-stage model Pb evolution curve composition at 300 Ma, ranging from 363.1 ± 0.6 Ma to 296.1 ± 0.5 Ma (Figure 8b). Apatite grains are quite radiogenic ($^{207}Pb/^{206}Pb$ <0.2), making the choice of initial Pb composition less relevant for most analyses, considering the uncertainty on the individual dates calculated. Two other apatite crystals yielded $^{206}Pb/^{238}U$ ages of 702 ± 2 Ma which are strongly inversely discordant (and is not further discussed in this contribution) and 166.4 ± 0.5 Ma, which is slightly normally discordant. In order to date the Beauvoir intrusion emplacement, analyses yielding an age between 309 and 318 Ma were retained (solid ellipses and rectangles on Figure 8a) as this time interval is consistent with the previous dating performed on the Beauvoir granite (Cheilletz et al., 1992; Melleton et al., 2015; Rocher et al., 2024). These selected concordant apatite grains give a concordia age of 314.6 ± 0.1 (1.1) Ma (Figure 8a). When plotted in the Tera-Wasserburg space, these selected concordant apatite grains may give a date at 317.5 ± 3.8 Ma (Figure S3), overlapping with the $^{206}Pb/^{238}U$ concordia age. This age at 317.5 ± 3.8 Ma is however strongly biased by a single weakly radiogenic analysis (Figure S.3) and the $^{206}Pb/^{238}U$ age at 314.6 ± 0.1 (1.1) Ma will be preferred in this manuscript. As for the zircon analyses, the apatite measurement accuracy is controlled by their Pb_c/Pb^* ratio, where the more accurate analyses are those with a weak Pb_c/Pb^* (Figure 8a). Overall, the resulting age is similar for zircon and apatite within the uncertainty.

5 Discussion

5.1 Origin of the Beauvoir zircon

5.1.1 Zone 1: A magmatic origin

The Beauvoir zircon crystals are composed of two distinct domains: Zone 1 characterised by both rounded isolated pieces within Zone 2 as well as continuous growth zones that likely correspond to primary growth zones (e.g., Figure 3c). The Zone 1 tetrahedral site (T-site) is almost exclusively occupied by Si whereas the eightfold site (A-site) is filled by Zr together with minor Hf (**Erreur ! Source du renvoi introuvable.**). The hafnon substitution is commonly observed in zircon from differentiated bodies (Neves et al., 1974; Wark and Miller, 1993; Breiter et al., 2006; Claiborne et al., 2006; Abdalla et al., 2009; Van Lichtervelde et al., 2009; Wang et al., 2010; Breiter and Škoda, 2012). The relatively high hafnium concentration and variations in the Zr/Hf ratio in Zone 1 likely reflect the parental melt composition or changes crystallisation kinetics (e.g., dendritic growth; Gillespie et al., 2024). From their experimental work, Linnen and Keppler (2002) showed that Hf is less compatible in zircon, leading to an decrease of the Zr/Hf of the residual melt and an increase in hafnium concentration in zircon during fractionation. Therefore, the relatively high hafnium concentration in Beauvoir zircon would be related to the highly differentiated nature of the Beauvoir magmas whereas the Zr/Hf variations in each crystal would be the result of zircon growth from magmas at degree of differentiation.

Uranium was also incorporated in significant amount (on average 1.0 wt.% UO_2; **Erreur ! Source du renvoi introuvable.**) during zircon crystallisation, their protracted disintegration progressively damaged the crystal structure of Zone 1 to potentially form strongly disordered crystal. Although the average α-dose experienced by Zone 1 ($8.5.10^{15}$ α-decays/mg) is higher than the limit of 8.10^{15} α-decays/mg that defines a complete aperiodic crystal (Murakami et al., 1991), the high ν_3 (SiO_4) intensity and relatively low ν_3 (SiO_4) linewidth (< 20 cm^{-1}; Figure 6h and Figure 7a-c) of some Zone 1 zircons strongly suggest that the crystal lattice of these zircons is only weakly to moderately disordered. On the other hand, Zone 1 zircon with high ν_3 (SiO_4) linewidth (above 25 cm^{-1}; Figure 6h and Figure 7a-c) eventually corresponds to metamict zircon. Thus, Zone 1 corresponds to both weakly to moderately damaged zircon and metamict/aperiodic zircon, evolution that is represented by the linear trend in Figure 7b. Taking Zone 1 zircon as the whole, we would estimate an amorphous fraction of ~80% for Zone 1 zircon from the relationship between the α-dose experienced by a zircon and its amorphous fraction published by Nasdala et al. (2001).

5.1.2 Zone 2: A hydrothermal origin

Zone 2 is represented by a continuous and interconnected matrix in which fragments of Zone 1 are embedded. Zone 2 T-site is notable enriched in Al and P cations (0.05 and 0.11 apfu; **Erreur ! Source du renvoi introuvable.**) whereas the A-site notably contains elevated Ca and U cations (0.06 and 0.03 apfu; **Erreur ! Source du renvoi introuvable.**). This Si deficiency in Zone T-site is partially linked to the berlinite substitution: $2\ Si^{4+} \leftrightarrow P^{5+} + Al^{3+}$. The left-over P incorporated the zircon structure via the brabantite substitution: $2\ Si^{4+} + 2\ Zr^{4+} \leftrightarrow Ca^{2+} + (U^{4+}) + 2P^{5+}$, which also explain the Zr deficiency in the

Zone A-site. If the incorporation of Al and P in Zone 2 zircon are fully explained by the berlinite and berlinite/brabantite substitutions, an excess Ca has to have incorporated Zone 2 in another way. Uranium incorporation into zircon can only be partly explained by the coffinite substitution as zircon data plot below the 1:1 substitution vector (Figure 4g). As for calcium, additional uranium eventually entered the zircon crystal lattice through the brabantite substitution. Incorporation of low-field strength cations (e.g., Fe and Mn) in zircon structure is more complex to assess. Considering only the valence on these cations, they could substitute Zr in the eightfold site (A-site) via the coupled substitution $Zr^{4+} \leftrightarrow 2\ (Mn^{2+} + Fe^{2+})$(Figure 4h). However, such substitution seems to be impossible considering the $Zr^{[8]}$ ionic radii (0.84 Å; Shannon, 1976) with the one of $Mn^{2+\,[8]}$ and $Fe^{2+\,[8]}$ (respectively 0.96 and 0.92; Shannon, 1976). From their study on similar zircons, Pérez-Soba et al. (2014) proposed that $Fe^{2+\,[4]}$ together with $O^{2-\,[4]}$ could enter in the four-coordinated interstitial (1.84 Å; Finch et al., 2001) site as the sum of their ionic radii is 2.01 Å (Shannon, 1976). Mn could substitute Zr in the zircon A-site as also proposed by Pérez-Soba et al. (2014). Fluorine is likely localised in the zircon T-site as F negatively correlates with Si (Figure 4e) potentially involving a substitution $(SiO_4)^{4-} \leftrightarrow (F_4)^{4-}$. This fluorine incorporation in the zircon T-site was already experimentally identified by Caruba et al. (1985) who synthetised hydrous zircon with up to 0.8 apfu $(OH,F)_4$ substituting the SiO_4 group. Another way to incorporate anions (i.e., OH^-, F^- and Cl^-) in zircon structure has for instance been proposed by Courtney-Davies (2019) in their study on metasomatic zircon in gold-copper granite deposits where O^{2-} would be substituted by 2 (OH^-, Cl^-). In addition, it should be noted that the substitution game that experienced these zircons has a “snow-ball effect”. Indeed, the first substitution of P+Al in the T-site strongly disordered the early-formed zircon crystal structure. This lattice was eventually more disordered after the Ca and U incorporation in the A-site. Thus, it is also highly possible that other substituting elements (e.g., the Ca excess and other trace element) entered the highly disordered zircon lattice in interstitial position apart from the main lattice sites (e.g., Finch et al., 2001; Breiter and Škoda, 2012). Caruba et al. (1985) also noticed that the ν_3 (SiO_4) peak position of hydrous zircon is shifted to higher wavelength when compared to pure zircon (1020 to 1045 cm^{-1}). On the other hand, the protracted alpha-decay and zircon lattice damage leading to a metamict state is associated with an overall decrease in Raman band intensity as well as a shift to lower wavenumbers (e.g., Nasdala et al., 2001 and Figure 7c). Thus, although Zone 2 corresponds to metamict zircon, the fact that its ν_3 (SiO_4) peak position is not that different from the one characterising Zone 1 (Figure 7a) could be explained by the presence of water in the aperiodic Zone 2 structure. However, a spectroscopic analysis (e.g., Raman) on a complete aperiodic mineral should, by definition, leads to a flat spectrum (i.e., without peak), which is not what we observe in Zone 2 Raman spectra (Figure 6g-i and Figure 7a-c). A potential alternative would be that the apparent ν_3 (SiO_4) peak between 990 and 996 cm^{-1} is actually not only related to the SiO_4 tetrahedra vibrations but to the PO_4 tetrahedra vibration. Indeed, considering the important phosphorus concentration in Zone 2 zircon and the fact that the A_{1g} (PO_4) vibrational band typically ranges between 985 and 1000 cm^{-1} (e.g., Švecová et al., 2016), it is likely that the observed peak in Zone 2 spectra can account for both SiO_4 and PO_4 tetrahedra vibrations. Highly metamict zircon containing up to 16.6 wt.% H_2O has been described by Coleman and Erd (1961). The low oxide sum in Zone 2 would thus be related to the absence of water quantification via EPM analyses, as already inferred by Breiter & Škoda (2012). The incorporation of aluminium together with phosphorus in the zircon T-site, reflecting the berlinite substitution, was proposed by Breiter et al. (2006) to be a primary magmatic feature reflecting zircon crystallisation from a phosphorus and alumina-rich melt. On the other hand, elevated calcium concentrations in zircon (> 2 wt.% CaO) were attributed to zircon alteration by low-temperature fluids (Geisler and Schleicher, 2000).

The textures and chemical composition of Zone 2 raise the question of its origin (i.e., magmatic and/or hydrothermal). A fully magmatic origin would imply that Zone 2 zircon crystallised from a compositionally different melt (or under very different physical conditions) than that from which Zone 1 crystallised. Such a melt would have to be strongly enriched in U, P, Al, F, C, Fe and Mn compared to the parental melt of Zone 1. Although extreme magmatic differentiation of the Beauvoir magmas has led to the formation of P-, Al- and F-rich residual liquids, this differentiation also induced melt depletion in Fe, Mn and Ca (Esteves et al., 2024). Since Fe, Mn and Ca are positively correlated with P and F in Zone 2, the compositional variations cannot be linked to melt differentiation. Moreover, extreme fractionation would also have led to the formation of Hf-rich residual melt (Linnen and Keppler, 2002; Zaraisky et al., 2008; Wang et al., 2010). This is not recorded by Zone 2 zircon, which is on average less enriched in Hf compared to Zone 1 zircon (Fig. 4d). Thus, a magmatic origin for Zone 2 is inconsistent with the observed concentrations and other processes must have taken place.

It is well documented that the Beauvoir rare-metal magmas experienced numerous stages of fluid exsolution prior to their complete solidification (~550 °C; Pichavant, 2022), as numerous fluid/brine inclusions mainly in quartz and topaz have been reported throughout the granite (Aïssa et al., 1987; Fouillac et al., 1987; Harlaux et al., 2017; Rocher et al., 2024). Based on a fluid inclusion study, Harlaux et al. (2017) showed that a first generation of exsolved brines (L1: 17-28 wt.% NaCl eq.) from the Beauvoir silicate magma occurred during magma crystallisation (from >600 to 500 °C). This first generation is enriched in Na, Li, K, Al, Mn, Fe and F compared to the Beauvoir magmas (Aïssa et al., 1987; Harlaux et al., 2017). As hydrothermal apatite also precipitated from these fluids (Rocher et al., 2024), they were also eventually enriched in Ca and P. Once Beauvoir magmas completely solidified, numerous fluids and brines generations continued to circulate through the Beauvoir granite (see details in Aïssa et al., 1987; Fouillac et al., 1987; Harlaux et al., 2017; Rocher et al., 2024) during its progressive cooling. From leaching experiments, Geisler et al. (2002) demonstrated the capacity of low-temperature chloride-bearing fluids to leach metamict zircon containing an amorphous fraction of 85% (~0.59.10^{16} α-decays/mg which is slightly more than the half of the actual Zone 1 zircon). Such interaction efficiently removed the Si^{4+} and Zr^{4+} cations from metamict zircon with subsequent replacement by Al^{3+} and Ca^{2+}. Such replacement processes are a common feature in zircons in highly differentiated systems that have experienced hydrothermal alteration (e.g., Černý and Siivola, 1980; Uher and Černý, 1998; Geisler et al., 2002, 2007; Van Lichtervelde et al., 2009; Breiter and Škoda, 2012; Troch et al., 2018; Courtney-Davies et al., 2019; Han et al., 2023). Therefore, the continuous trends between Zone 1 and Zone 2 composition (Figure 4a-i) could potentially be explained by various replacement degrees of Zone 1 by Zone 2 material through reactions with deuteric fluids and/or melts.

In order to evaluate if such a replacement occurred, we need constrain how damaged the zircons were during the circulation of these chloride-bearing hydrothermal fluids. Although the duration of the Beauvoir hydrothermal activity is not well constrained, Charoy et al. (2003) estimated a maximum duration of a few million years, which is consistent with the age of the Beauvoir hydrothermal apatite (Apatite II; 314.3 ± 5.5 Ma and 311.7 ± 8.1 Ma; Rocher et al., 2024). Assuming a hydrothermal activity duration of 5 Ma, Zone 1 would have experienced ~$1.3.10^{14}$ α-decays/mg after these 5 Ma which would correspond to fully crystalline zircon (Murakami et al., 1991; Nasdala et al., 2001). Although Zone 1 zircon was ~40 times less damaged than the zircon used by Geisler et al. (2002), their leaching experiments were conducted at 175 °C for 1340 h. Such conditions are far from what the Beauvoir zircons experienced with a fluid temperature of 400-600 °C (Harlaux et al., 2017) and a potential duration of a few millions of years (Charoy et al., 2003). Thus, it is likely that Zone 1 zircon was partially leached by reactive chloride-bearing fluids during the Beauvoir hydrothermal activity, resulting in the Zone 2 formation (Figure 9b).

Based on the compositional analyses of the Beauvoir L1 fluid inclusions (LA-ICP MS; Harlaux et al., 2017), these hydrothermal fluids were 10 to 100 times more enriched in Fe and Mn than the Beauvoir silicate magmas.. The elevated incorporation of Fe and Mn cations in Zone 2 would be related to these Fe- and Mn-rich fluids, a process also identified in other metasomatic zircon by Courtney-Davies et al.(2019). An external source of Fe^{2+} and Mn^{2+} via the meteoritic water influx is possible as well, as they partially leached the host micaschist before interacting with the Beauvoir magmas (Charoy et al., 2003; Harlaux et al., 2017; Rocher et al., 2024). Although P, Al, Ca and F concentrations in the Beauvoir fluid inclusions are unknown, the ubiquitous presence of hydrothermal apatite, topaz and fluorite in Beauvoir greisens (Monnier et al., 2020; Rocher et al., 2024) supports the high P, Al, Ca and F concentrations in these hydrothermal fluids. Part of this Ca could derived either from the alteration of magmatic plagioclase or from the leaching of the host micaschist (Charoy et al., 2003). The leaching of uranium-bearing oxides if often considered to explain the U-rich nature of hydrothermal fluids in leucogranites (e.g., Dolníček et al., 2014; Ballouard et al., 2017; Rocher et al., 2024). In the Beauvoir granite, U could either have been derived from the breakdown of magmatic pyrochlore as it experienced a significant U^{4+} removal during the Beauvoir magmatic-hydrothermal transition (Ohnenstetter and Piantone, 1988), or derived from the leaching of early formed uraninite (Cuney and Brouand, 1987). Therefore, it is most likely that the formation of the P-, Al-, Fe-, Mn-, Ca-, U- and F-rich Zone 2 is associated with the progressive replacement of Zone 1 zircon by reactive hydrothermal fluids (Figure 9b). Such replacements started at the Beauvoir magmatic-hydrothermal transition (i.e., under the presence of residual melts) and ceased once the Beauvoir hydrothermal activity ended (or when these fluids were not reactive anymore in respect to zircon grains; Figure 9d). As shown by the zircon in Figure 3c, some continuous Zone 1 growth zones have not been replaced (e.g., the one containing cracks). This feature indicates that the original zircon (i.e., before its partial replacement) composed of Zone 1 material, was not homogeneous (Figure 9a), and some growth zones were more prone than others to be replaced (e.g., Černý and Siivola, 1980; Geisler et al., 2007; Van Lichtervelde et al., 2009). Such differences in the original zircon likely correspond to compositional variations that are directly linked to lattice ordering (Finch et al., 2001; Geisler et al., 2006) and so, to the resistance against reactive fluids (Černý and Siivola, 1980; Geisler et al., 2007). Indeed, in their study on high-U zircon that crystallised from the Chernobyl “lavas”, Geisler et al. (2006) showed that high uranium incorporation in zircon is the source of microscopic strain within the zircon crystal structure. This strain is directly related to the size of U^{4+}, which is ~16% larger than Zr^{4+} (Shannon, 1976). A same conclusion was drawn by Finch et al. (2001) where they observed that xenotime substitution in zircon ($Zr^{4+} + Si^{4+} \leftrightarrow REE^{3+} + P^{5+}$) is associated with an increase in lattice strain. Thus, primary enriched (e.g., U- and/or trace element-rich) Zone 1 would have started to be preferentially dissolved and replaced at the magmatic-hydrothermal transition due their more disordered crystal structure. The growth zones that are poorer in U and/or in trace elements as the one in Figure 9a resisted to these reagents and acted as a shield for zircon cores (e.g., Figure 3c). Phosphorus-rich fractures that are contained in these growth zones likely indicate that the reactive fluids entered the zircon cores by fracturing those growth zones (Figure 3a-e). Such fractures that were also observed by Geisler et al. (2002) in their leaching experiments acted as a pathway for the reactive fluids, allowing the progressive replacement of the zircon core. As these fractures are also connected to muscovite and quartz inclusions (Figure 3d), it is most likely that these hydrothermal minerals that are common in Beauvoir greisen (Monnier et al., 2022; Rocher et al., 2024) crystallised at the same time as Zone 2 was formed (Figure 9c).

Once the Beauvoir hydrothermal activity ceased, the radionuclides contained in the Beauvoir zircons (mainly U) progressively damaged both Zone 1 and 2 due to their prolonged disintegration, leading to an almost amorphous Zone 1 and a completely amorphous Zone 2 (Figure 9d). Additional elements might have migrated into and out of these amorphous and metamict zircon grains since more than 300 Ma (Figure 9d) as element diffusivity in amorphous material is strongly higher than the one in pristine material (e.g., Cherniak et al., 1991; Geisler et al., 2003, 2007). As such, the complex composition of Beauvoir zircon is a combination of both their hydrothermal alteration and their subsequent element incorporation in relation with their progressive amorphisation.

5.1.3 Origin of Zr-5

The zircon grain Zr-5 is texturally different from the other Beauvoir zircons in that it does not present isolated Zone 1 zircon within Zone 2 material (Figure 10a). In Zr-5, the inner zone (i.e., core) is characterised by a Si-rich zircon (Figure 10b) containing numerous uraninite micro-inclusions (Figure 10a, c). The distribution of these inclusions is not homogeneous, and they are absent in the P-rich area (Figure 10d). On the other hand, the Zr-5 rim, which contains no uraninite inclusions, is zoned with a progressive decrease in U content (from ~5.5 to < 1 wt.% UO_2; Figure 10c) towards the crystal rim. These U variations are not associated with Si or P variations (Figure 10b-d), suggesting that U was not incorporated through a brabantite substation. On the other hand, U in Zr-5 is negatively correlated with Zr which supports uranium incorporation via the coffinite substitution (Figure 4g). Although the Zr-5 data do not strictly fall on the $Zr^{4+} = U^{4+}$ substitution vector, they are parallel to this vector at lower Zr value (Figure 4g) reflecting another substitution involving Zr such as the hafnon substitution ($Zr^{4+} = Hf^{4+}$) as Zr-5 contain ~3 wt.% HfO_2 (Figure 4f). Even if Zr-5 zircon is unique, its outer rim is compositionally similar to Zone 1 (Figure 4e-i). Some local domains are enriched in P and depleted in Si (Figure 10b, d), which eventually reflect the berlinite and brabantite substitution (Figure 4a-d) during episodes of zircon alteration under reactive hydrothermal fluids. These Zr-5 alteration episodes were however much more limited than for the other zircon grains presenting the interconnected Zone 2 material. Thus, Zr-5 likely represents the Beauvoir zircons that have not undergone intense alteration by reactive hydrothermal fluids. An early zircon crystallisation stage would have formed U-rich zircon, while magmatic differentiation triggered U melt depletion, as evidenced by the U-poor nature of Zr-5 rims (Figure 10c). Following this protracted magma crystallisation, Zr-5 experienced limited alteration from reactive fluids (Figure 10f) leading to the formation of phosphorus-rich regions in replacement of the original Zr-5.

The origin of the uraninite inclusions in Zr-5 is more difficult to assess. Three main hypotheses could explain the presence of these inclusions: A contemporaneous uraninite growth with the zircon, uraninite precipitation during zircon dissolution-reprecipitation under reactive hydrothermal fluids (e.g., Geisler et al., 2007; Troch et al., 2018), or by secondary exsolution. Although subhedral uraninite is present in the Beauvoir granite (Cuney and Autran, 1988), the fact that it is absent from all other studied zircons suggests that co-crystallisation prior to their entrapment is highly unlikely. Moreover, most inclusions have sigmoidal shape (Figure 10a), in disagreement with the expected cubic shape if uraninite had crystallised from a melt. The presence of such inclusions in spongy zircon has also been proposed to be linked with dissolution-reprecipitation processes with hydrothermal fluids (e.g., Hetherington and Harlov, 2008 in xenotime and Troch et al., 2018; Monnier et al., 2024 in zircon). For instance, the presence of rounded U-rich thorite, yttrialite and uraninite inclusions in metamict and spongy zircon from Yellowstone rhyolites were attributed by Troch et al. (2018) to result from 1) the dissolution of metastable U-Th-rich zircon and 2) the simultaneous reprecipitation of these inclusions with a stable U-Th-poorer zircon. Although we showed that Beauvoir zircon grains were replaced by reactive hydrothermal fluids forming Zone 2 zircon (Figure 9b), these Zone 2 domains do not contain these uraninite micro-inclusions. In addition, as the P-rich, altered parts of Zr-5 are those that do not contain these uraninite micro-inclusions (Figure 10a and d), it is unlikely that these inclusions are associated with dissolution-reprecipitation processes.

We therefore favour the third hypothesis, whereby uraninite formed by exsolution from U-rich core, corresponding to the early U-rich Zr-5 crystallisation (Figure 10e). Since Zr^{4+} is ~16% smaller than U^{4+} (Shannon, 1976), the coffinite substitution is not ideal, and a miscibility gap exists between coffinite and zircon end-members (Ferriss et al., 2010). Based on solubility experiments, Ushakov et al. (1999) determined that the maximum $USiO_4$ solubility in zircon is less than 6 % mol. at 1400-1500 °C, corresponding to a concentration of ~8.9 wt.% UO_2. This maximum solubility is likely to decrease at lower crustal temperatures (<500 °C). This lack of exsolution texture in zircon might be the result of slow U^{4+} diffusion in zircon ($6.8.10^{-29}$ $m^2.s^{-1}$ at 1100 °C; Cherniak et al., 1997) and therefore, U-rich zircons (>9 wt.% UO_2) would correspond to metastable crystals (Geisler et al., 2007; Ferriss et al., 2010; Troch et al., 2018). However, it has been shown that the elemental diffusivity in metamict zircon, in which a significant part of the crystal is amorphous and material-depleted, is significantly faster than in a crystalline zircon (e.g., Cherniak et al., 1991; Geisler et al., 2003, 2007). Thus, it seems possible that uranium mobility in amorphous material would ideally create sites of exsolved U-bearing phases (uraninite or coffinite). Following this, the Zr-5 uraninite micro-inclusions (Figure 10a) would have been formed via a uranium exsolution promoted by the intense amorphisation of the zircon crystal structure (Figure 10g). Thus, the sharp boundary between the Zr-5 core and its rim (Figure

10a-g) would potentially reflect the U concentration threshold at which uranium exsolution occurred in Beauvoir zircon grains (~6 wt.% UO_2; Figure 10c). The absence of these UO_2 exsolution in the P-rich and replaced Zr-5 core would thus be linked to dissolution-reprecipitation process (e.g., Troch et al., 2018) where U-poorer zircon would have replaced the originally U-rich zircon. Using simple image processing, the Zr-5 core is composed of ~11% of exsolved uraninite and ~89% of zircon. Considering a concentration of 100 wt.% UO_2 in uraninite and 6 wt.% UO_2 in zircon, the original composition of Zr-5 core after its crystallisation would be ~16.3 wt.% UO_2. Such a concentration is far above that in Beauvoir Zone 1 zircons, thus indicating that the Zr-5 core does not correspond to Zone 1, and must have crystallised earlier as uranium behaves compatibly in such evolved magmas. On the contrary, Zr-5 rim could correspond to the preserved Zone 1 zircon.

5.2. Beauvoir geochronology

5.2.1 Zircon lattice damage inducing lead loss

All but one of the Beauvoir analysed zircons form a discordia line, witch upper intercept represents their crystallisation age (Figure 8a). The fact that the origin of the discordia is anchored at the origin of the Wetherill plot (Figure 8a) indicates that these zircons have experienced continuous lead loss since their crystallisation as a result of their metamict lattice state (Mezger and Krogstad, 1997; Figure 9b-d). On the other hand, no effect of the late Permian and Jurassic hydrothermal circulations, which has been identified with Beauvoir apatite (Rocher et al., 2024), is identified here. As mentioned above, both Zone 1 & 2 are highly damaged due to their high uranium concentration. Based on molecular-dynamics simulations, Geisler et al. (2003b) showed that the accumulation of radiation damage can form interconnected regions of amorphous and depleted matter, which promotes element diffusivity through these depleted regions. Two main thresholds have been identified during a progressive zircon amorphisation (Salje et al., 1999; Geisler et al., 2003). The first threshold is reached when the amorphous domains are interconnected at the crystal scale (~30% of amorphous domains). The second threshold, corresponding to a higher amorphisation degree (~70%), is reached when the crystalline materials are no longer connected and form isolated crystalline islands in an amorphous environment. In order to quantify when these thresholds were reached for both Beauvoir Zone 1 and 2, we calculated the number of α-decays/mg that these zircons have undergone since their crystallisation at ca. 314.6 Ma (Figure 11a). To do so, the initial U concentration of both Zone 1 and 2 has been calculated based on their averaged U present day concentration (**Erreur ! Source du renvoi introuvable.**). The progressive α-decay events experienced by Zones 1 and 2 were then modelled based on the U radioactive decay of Jaffey et al. (1971). Although simplistic, these models eventually simulate, in the first order, the evolution of Zone 1 and 2 crystal structure through time. At ***t*** = 0 (i.e., 314.6 My ago), radionuclide decay had just started and thus, their mesoscopic structure was fully crystalline (Figure 11a-b). The first threshold was reached after ~150 Ma for zone 1, whereas it was attained after ~45 Ma for Zone 2 (Figure 11a). Such a difference is easily explained by their different U concentrations (**Erreur ! Source du renvoi introuvable.**). The second threshold, corresponding to isolated crystalline zircon within an amorphous material, was reached after 285 Ma for Zone 1 and after 80 Ma for Zone 2 (Figure 11a). At this point, most of the crystal is amorphous, further enhancing the processes of elemental mobility and lead loss. Such results imply that analysed Beauvoir zircons that are composed predominantly of Zone 2 material eventually experienced more radiogenic lead loss than those composed predominantly of Zone 1 material. These proportional differences would therefore be at the origin of variations in the degree of discordance of the Beauvoir zircons (Figure 8a).

5.2.2 The apatite record and other dating methods

Concordant apatite ages spread from 363.2 ± 0.6 to 296.2 ± 0.5 Ma (Figure 8b), potentially indicating that various apatite populations crystallised during different magmatic episodes. The main apatite population has $^{206}Pb/^{238}U$ ages ranging from 309.6 ± 0.5 to 317.7 ± 0.5 Ma with a concordant age at 314.6 ± 0.1 (1.1) Ma which likely corresponds to the Beauvoir crystallisation age. This age is similar to the one obtained with larger uncertainties by Rocher et al. (2024) on magmatic apatite (Apatite I) at 314.6 ± 3.5 Ma, which is also within the uncertainty of our ages from Beauvoir zircon (312.0 ± 2.9 (7.2) Ma) as well as the age obtained by Melleton et al. (2015) at 317 ± 6 Ma using the U-Pb method on columbite-tantalite. However, this apatite age is significantly younger than the zircon age reported from Beauvoir microgranite ($Zr_{\mu G}$: 323 ± 4 Ma – U/Pb, LA-ICP MS; Monnier, 2018) and conversely, significantly older than the age obtained on Beauvoir lepidolite (308 ± 2 Ma – Ar-Ar; Cheilletz et al., 1992). Four older concordant apatite grains have crystallisation ages of 323.6 ± 0.4, 329.1 ± 0.6, 337.6 ± 0.6 and 363.1 ± 0.6 Ma (Figure 8b) and could either correspond to an artefact linked to U-mobility in these apatite crystals or to apatite antecrysts/xenocrysts. Although bluish (i.e., magmatic) apatite grains were carefully handpicked, older apparent ages could be the result of U mobility under the presence of hydrothermal fluids. Moreover, it has been shown that thermally activated volume diffusion of Pb in apatite can locally create domains that are apparently older than formation ages if U is zoned (e.g., Paul et al., 2019; Popov et al., 2020). Therefore, as we may have analysed fragments of apatite (i.e., due to the rock fragmentation) combined with the intense hydrothermal activity that occurred at Beauvoir, it may well be that U-mobility between these apparent old apatite grains and fluids is at the origin of these older dates, making them geologically meaningless. In addition, such partial opening of these apatite U-Pb isotopic systems would thus be at the origin of the scatter observed in the Tera-Wasserburg space when compared with the selected apatite population from which the Beauvoir crystallisation age has been determined (Fig. S3). Nevertheless, we cannot conclude or exclude if such U-mobility in these older apatite grains actually occurred. Another explanation would be that the older apatite ages represent antecrysts and/or xenocrysts. Indeed, the early crystallisation of apatite in Beauvoir magmas, which is attested by their inclusion in early-formed topaz (Rocher et al., 2024), indicates that Beauvoir melts were eventually saturated in phosphorus at the time of their intrusion into the Beauvoir reservoir. The uptake of apatite antecrysts and xenocrysts by such phosphorus-saturated melts during their ascent through the magmatic plumbery would thus theoretically prevent their dissolution (although it might slightly disturb their U-Pb system). As such, the 323.6 Ma apatite could have crystallised during the same magmatic episode than ZrμG while older apatite grains may be associated with previous magmatic events that occurred within the Sioule area such as the Pouzol-Servant magmatism at ca. 330 Ma (Pin, 1991) as well as older gneisses belonging to the upper gneiss unit (ca. 350-360 Ma; Do Couto et al., 2016). However, it is not possible to invoke a recycling process to account for the presence of the 296 Ma concordant apatite. Such apatite might have experienced localised late fluid circulation that reopened its isotopic system and may be associated with the late Permian hydrothermal fluid circulation event identified by Rocher et al. (2024) at 268.3 ± 20.4 Ma.

5.3 Implications for dating rare-metal granites

Although the use of U-Pb CA-ID-TIMS geochronology on zircons is so far the most accurate technique to constrain when and how long a plutonic assembly occurred (e.g., Schoene et al., 2012; Schaltegger et al., 2021), its use in highly differentiated systems such as rare-metal granites and pegmatites is limited due to the high uranium concentration of zircon, associated decay-related damage and ubiquitous lead loss. Moreover, as highlighted by the present, hydrothermal activity, which is common in such differentiated systems, strongly modifies original magmatic zircons and disturbs their isotopic signature. For a moderately damaged zircon grains without significant interaction with hydrothermal fluids, this issue can possibly be mitigated by chemical abrasion (e.g., McKanna et al., 2024; Schaltegger et al., 2024). For the strongly metamict zircons of the Beauvoir granite (~10^{16} α-dose/mg), the chemical abrasion step cannot discriminate between more and less damaged zircon domains because the entire grain is beyond the second threshold (>70% metamict domains; Figure 11). Thus, the use of high-precision zircon geochronology (CA-ID-TIMS) in such strongly differentiated systems is highly limited and restricted to the upper intercept calculation of a lead loss Discordia (Figure 8a).

On the other hand, since apatite is a common magmatic mineral in highly differentiated granites and pegmatites, combined with its closure temperature, the application of apatite geochronology allows us to acquire the most accurate Beauvoir emplacement age so far at 314.6 ± 0.1 (1.1) Ma (Figure 8b). For comparison, LA-ICP MS dating are associated with a higher uncertainty as illustrated with the ages obtained on the Beauvoir magmatic apatite, 314.6 ± 4.7 Ma (Rocher et al., 2024) and columbite-tantalite, 317 ± 6 Ma (Melleton et al., 2015). Further developments on high-precision ID-TIMS analyses of other U-bearing minerals such as cassiterite (e.g., Carr et al., 2020), wolframite (e.g., Romer and Lüders, 2006; Carr et al., 2021) or columbite-tantalite (e.g., Romer and Smeds, 1994; Yang et al., 2023) would likely increase our understanding of the emplacement and mineralisation processes related to highly-differentiated rare-metal silicic melts.

6 Conclusions

Zircons from the Beauvoir rare-metal granite are mostly composed of two distinct materials: Zone 1 and 2. Zone 1, which is Si- and Zr-rich directly crystallised from the Beauvoir silicate melt. The P-, Al-, F-, Ca-, Fe-, Mn- and U-rich Zone 2 zircon is attributed to partial replacement of Zone 1 by reactive hydrothermal chloride-bearing fluids. This partial replacement process has led to isolated rounded Zone 1 material within the interconnected Zone 2 material. Once the circulation of these fluids stopped, it took ~105 and ~45 Ma for Zone 1 & 2, respectively, to reach the point where amorphous domains are interconnected, whereas the second threshold where crystalline islands were isolated inside a metamict (i.e., amorphous) matrix was reached after ~285 and ~80 Ma for Zone 1 & 2, respectively. As a result, the entire volume of any Beauvoir zircon is almost completely amorphous today. Another zircon population containing several uraninite micro-inclusions likely documents for the first time uraninite exsolution in uranium-rich zircon. This uraninite exsolution was likely triggered by the primary uranium-rich composition before becoming oversaturated during the cooling of the Beauvoir system. Uranium migration was then enhanced by the advance zircon lattice disordering degree, allowing U^{4+} migration through the amorphous zircon.

Although we used the most accurate method for zircon geochronology (CA-ID-TIMS), the Beauvoir zircons were too damaged (i.e., metamict) to survive the chemical abrasion step. Analyses of the total dissolutions have led to a well aligned discordia with an upper intercept of 312 ± 2.9 (7.2) Ma. This age, within the uncertainty of previous Beauvoir dating, might reflect the end of the Beauvoir main reactive magmatic-hydrothermal activity (before subsequent reactivation at Permian and/or Jurassic times; Rocher et al., 2024). The high degree of discordance is related to extensive radiogenic lead loss since the zircon crystallisation. This radiogenic lead (in addition to other elements) efficiently diffused through zircon grains via elemental diffusion through interconnected pathways in amorphous materials. Compared to zircon geochronology, apatite U-Pb ID-TIMS analyses yield Beauvoir crystallisation age of 314.6 ± 0.1 (1.1) Ma, which is the most precise dating of the Beauvoir granite so far.

Thus, although zircon texture and chemical composition can provide significant insights into the magmatic-hydrothermal transition of highly differentiated systems such as rare-metal granites, their use to accurately date these objects is not the optimal approach. The combined primary U-rich nature inducing lattice damage and enhancing lead migration together with the partial replacement during the magmatic-hydrothermal transition strongly disturb their original U-Pb isotopic signature. We thus envision that alternative high-precision ID-TIMS method on other accessory minerals such as apatite would be more appropriate and appears to be a powerful tool for future studies aiming at obtaining a better understanding of the emplacement and mineralisation of such systems.

7 Data availability

All the data presented in this contribution are given in the supplement.

8 Author contribution

NE collected the samples, prepared them, carried the U-Pb chemistry as well as EPMA and micro-Raman analyses, analysed the data and wrote the first draft. PB, LF and US designed the research. MO and ANP assisted NE for U-Pb chemistry and carried the U-Pb analyses. All the authors participated in the elaboration of this contribution.

9 Competing interests

The authors declare that they have no conflict of interest.

10 Acknowledgements

This study, part of the BeauLiϒ project, was supported by the French National Research Agency through the national program “Investissement d’avenir” with the reference ANR-10-LABEX-21-RESSOURCES21 grant, and INSU/CNRS TelluS grant (2022) both given to P. Bouilhol. The authors acknowledge the DrEAM project given to N. Esteves from “Lorraine Université d’Excellence” at Université de Lorraine for the support of an international mobility to Geneva University (Switzerland). The authors want to thank Jérémie Melleton (BRGM) for assistance during borehole sampling at BRGM as well as the Steval (Georessources) team for their assistance using Selfrag instrument. Andreï Lecomte and Marie-Camille Caumon (Georessources) are also warmly thanked for their help and assistance respectively during electron probe micro-analyses and micro-Raman measurements. NE thanks Christophe Ballouard and Simon Couzinié for the fruitful discussions related to the Beauvoir zircons.

11 References

Abdalla, H.M., Helba, H., Matsueda, H., 2009. Chemistry of zircon in rare metal granitoids and associated rocks, Eastern Desert, Egypt. Resour. Geol. 59, 51–68.

Aïssa, M., Weisbrod, A., Marignac, C., 1987. Caractéristiques chimiques et thermodynamiques des circulations hydrothermales du site d’Echassières. Géologie Fr. 335–350.

Alekseev, V.I., Polyakova, E.V., Machevariani, M.M., Marin, Yu.B., 2014. Evolution of zircons from postorogenic intrusive series with Li-F granites, Russian Far East. Geol. Ore Depos. 56, 513–530. https://doi.org/10.1134/S1075701514070034

Annen, C., 2011. Implications of incremental emplacement of magma bodies for magma differentiation, thermal aureole dimensions and plutonism–volcanism relationships. Tectonophysics 500, 3–10. https://doi.org/10.1016/j.tecto.2009.04.010

Aubert, G., 1969. Les coupoles granitiques de Montebras et d’Echassières (Massif central français) et la génèse de leurs mineralisations en étain, lithium, tungstène et béryllium. Mém. BRGM Orléans 46, 349.

Ballouard, C., Poujol, M., Boulvais, P., Mercadier, J., Tartèse, R., Venneman, T., Deloule, E., Jolivet, M., Kéré, I., Cathelineau, M., Cuney, M., 2017. Magmatic and hydrothermal behavior of uranium in syntectonic leucogranites: The uranium mineralization associated with the Hercynian Guérande granite (Armorican Massif, France). Ore Geol. Rev. 80, 309–331. https://doi.org/10.1016/j.oregeorev.2016.06.034

Barboni, M., Annen, C., Schoene, B., 2015. Evaluating the construction and evolution of upper crustal magma reservoirs with coupled U/Pb zircon geochronology and thermal modeling: A case study from the Mt. Capanne pluton (Elba, Italy). Earth Planet. Sci. Lett. 432, 436–448. https://doi.org/10.1016/j.epsl.2015.09.043

Barboni, M., Schoene, B., Ovtcharova, M., Bussy, F., Schaltegger, U., Gerdes, A., 2013. Timing of incremental pluton construction and magmatic activity in a back-arc setting revealed by ID-TIMS U/Pb and Hf isotopes on complex zircon grains. Chem. Geol. 342, 76–93. https://doi.org/10.1016/j.chemgeo.2012.12.011

Bowring, J.F., McLean, N.M., Bowring, S.A., 2011. Engineering cyber infrastructure for U-Pb geochronology: Tripoli and U-Pb_Redux. Geochem. Geophys. Geosystems 12, 1–19. https://doi.org/10.1029/2010GC003479

Breiter, K., Förster, H.-J., Škoda, R., 2006. Extreme P-, Bi-, Nb-, Sc-, U- and F-rich zircon from fractionated perphosphorous granites: The peraluminous Podlesí granite system, Czech Republic. Lithos 88, 15–34. https://doi.org/10.1016/j.lithos.2005.08.011

Breiter, K., Škoda, R., 2012. Vertical zonality of fractionated granite plutons reflected in zircon chemistry: the Cínovec A-type versus the Beauvoir S-type suite. Geol. Carpathica 63, 383–398. https://doi.org/10.2478/v10096-012-0030-6

Carr, P.A., Mercadier, J., Harlaux, M., Romer, R.L., Moreira, E., Legros, H., Cuney, M., Marignac, C., Cauzid, J., Salsi, L., Lecomte, A., Rouer, O., Peiffert, C., 2021. U/Pb geochronology of wolframite by LA-ICP-MS; mineralogical constraints, analytical procedures, data interpretation, and comparison with ID-TIMS. Chem. Geol. 584, 120511. https://doi.org/10.1016/j.chemgeo.2021.120511

Carr, P.A., Zink, S., Bennett, V.C., Norman, M.D., Amelin, Y., Blevin, P.L., 2020. A new method for U-Pb geochronology of cassiterite by ID-TIMS applied to the Mole Granite polymetallic system, eastern Australia. Chem. Geol. 539, 119539. https://doi.org/10.1016/j.chemgeo.2020.119539

Caruba, R., Baumer, A., Ganteaume, M., Iacconi, P., 1985. An experimental study of hydroxyl groups and water in synthetic and natural zircons: a model of the metamict state. Am. Mineral. 70, 1224–1231.

Černý, P., 1992. Geochemical and petrogenetic features of mineralization in rare-element granitic pegmatites in the light of current research. Appl. Geochem. 7, 393–416. https://doi.org/10.1016/0883-2927(92)90002-K

Černý, P., Meintzer, R.E., Anderson, A.J., 1985. Extreme fractionation in rare-element granitic pegmatites; selected examples of data and mechanisms. Can. Mineral. 23, 381–421.

Černý, P., Siivola, J., 1980. The Tanco pegmatite at Bernic Lake, Manitoba. XII. Hafnian zircon. Can. Mineral. 18, 313–321.

Charoy, B., Chaussidon, M., Le Carlier De Veslud, C., Duthou, J., 2003. Evidence of Sr mobility in and around the albite–lepidolite–topaz granite of Beauvoir (France): an in-situ ion and electron probe study of secondary Sr-rich phosphates. Contrib. Mineral. Petrol. 145, 673–690.

Cheilletz, A., Archibald, D.A., Cuney, M., Charoy, B., 1992. Ages 40Ar/39Ar du leucogranite à topaze-lépidolit de Beauvoir et des pegmatites sodolithiques de Chédeville (Nord du Massif Central, France). Signification pétrologique et géodynamique. Comptes Rendus Académie Sci. Paris 315, 329–336.

Chelle-Michou, C., Chiaradia, M., Ovtcharova, M., Ulianov, A., Wotzlaw, J.-F., 2014. Zircon petrochronology reveals the temporal link between porphyry systems and the magmatic evolution of their hidden plutonic roots (the Eocene Coroccohuayco deposit, Peru). Lithos 198, 129–140.

Cherniak, D.J., Hanchar, J.M., Watson, E.B., 1997. Diffusion of tetravalent cations in zircon. Contrib. Mineral. Petrol. 127, 383–390. https://doi.org/10.1007/s004100050287

Cherniak, D.J., Lanford, W.A., Ryerson, F., 1991. Lead diffusion in apatite and zircon using ion implantation and Rutherford backscattering techniques. Geochim. Cosmochim. Acta 55, 1663–1673.

Claiborne, L., Miller, C.F., Walker, B.A., Wooden, J.L., Mazdab, F.K., Bea, F., 2006. Tracking magmatic processes through Zr/Hf ratios in rocks and Hf and Ti zoning in zircons: An example from the Spirit Mountain batholith, Nevada. Mineral. Mag. 70, 517–543. https://doi.org/10.1180/0026461067050348

Coleman, R., Erd, R., 1961. Hydrozircon from the Wind river formation, Wyoming. Short Pap. Geol. Hydrol. Sci. Artic. 147-292 Geol. Surv. Res. 1961 424, 297.

Condon, D.J., Schoene, B., McLean, N.M., Bowring, S.A., Parrish, R.R., 2015. Metrology and traceability of U–Pb isotope dilution geochronology (EARTHTIME Tracer Calibration Part I). Geochim. Cosmochim. Acta 164, 464–480. https://doi.org/10.1016/j.gca.2015.05.026

Courtney-Davies, L., Ciobanu, C.L., Verdugo-Ihl, M.R., Slattery, A., Cook, N.J., Dmitrijeva, M., Keyser, W., Wade, B.P., Domnick, U.I., Ehrig, K., Xu, J., Kontonikas-Charos, A., 2019. Zircon at the Nanoscale Records Metasomatic Processes Leading to Large Magmatic–Hydrothermal Ore Systems. Minerals 9, 364. https://doi.org/10.3390/min9060364

Cuney, M., Autran, A., 1988. Le forage scientifique d'Echassières (Allier). Une clé pour la compréhension des mécanismes magmatiques et hydrothermaux associés aux granites à métaux rares. Thème 8 : évolution d'un apex granitique. Doc. BRGM 437.

Cuney, M., Autran, A., Burnol, L., 1985. Programme Géologie profonde de la France. Troisième phase d'investigation : 1985-1986. Thème 8: Evolution géochimique et métallogénique d'un apex granitique (Echassières). Doc. BRGM 167.

Cuney, M., Brouand, M., 1987. Minéralogie et géochimie de U et Th dans le granite de Beauvoir et les micaschistes encaissants, comparaison avec la géochimie de l'étain. Geol. Fr. 247–257.

Cuney, M., Marignac, C., Weisbrod, A., 1992. The Beauvoir topaz-lepidolite albite granite (Massif Central, France); the disseminated magmatic Sn-Li-Ta-Nb-Be mineralization. Econ. Geol. 87, 1766–1794. https://doi.org/10.2113/gsecongeo.87.7.1766

Dawson, P., Hargreave, M.M., Wilkinson, G.R., 1971. The vibrational spectrum of zircon ($ZrSiO_4$). J. Phys. C Solid State Phys. 4, 240–256. https://doi.org/10.1088/0022-3719/4/2/014

De Saint-Blanquat, M., Habert, G., Horsman, E., Morgan, S.S., Tikoff, B., Launeau, P., Gleizes, G., 2006. Mechanisms and duration of non-tectonically assisted magma emplacement in the upper crust: The Black Mesa pluton, Henry Mountains, Utah. Tectonophysics 428, 1–31. https://doi.org/10.1016/j.tecto.2006.07.014

Do Couto, D., Faure, M., Augier, R., Cocherie, A., Rossi, P., Li, X.-H., Lin, W., 2016. Monazite U–Th–Pb EPMA and zircon U–Pb SIMS chronological constraints on the tectonic, metamorphic, and thermal events in the inner part of the Variscan orogen, example from the Sioule series, French Massif Central. Int. J. Earth Sci. 105, 557–579. https://doi.org/10.1007/s00531-015-1184-0

Dolníček, Z., René, M., Hermannová, S., Prochaska, W., 2014. Origin of the Okrouhlá Radouň episyenite-hosted uranium deposit, Bohemian Massif, Czech Republic: fluid inclusion and stable isotope constraints. Miner. Deposita 49, 409–425. https://doi.org/10.1007/s00126-013-0500-5

Drabon, N., Kirkpatrick, H.M., Byerly, G.R., Wooden, J.L., 2024. Trace elements in zircon record changing magmatic processes and the multi-stage build-up of Archean proto-continental crust. Geochim. Cosmochim. Acta 373, 136–150. https://doi.org/10.1016/j.gca.2024.03.014

Esteves, N., Bouilhol, P., Cuney, M., France, L., 2024. Small pluton construction through sills stacking, amalgamation and differentiation: Insight from the Beauvoir granite (Massif Central, France). Prepr. EarthArXiv Sumbitted J. Petrol. https://doi.org/10.31223/X5KT5V

Farina, F., Weber, G., Hartung, E., Rubatto, D., Forni, F., Luisier, C., Caricchi, L., 2024. Magma flux variations triggering shallow-level emplacement of the Takidani pluton (Japan): Insights into the volcanic-plutonic connection. Earth Planet. Sci. Lett. 635, 118688. https://doi.org/10.1016/j.epsl.2024.118688

Faure, M., Grolier, J., Pons, J., 1993. Extensional ductile tectonics on the Sioule metamorphic series (Variscan French Massif Central). Geol Rundsh 461–474.

Faure, M., Lardeaux, J.-M., Ledru, P., 2009. A review of the pre-Permian geology of the Variscan French Massif Central. Comptes Rendus Geosci. 341, 202–213. https://doi.org/10.1016/j.crte.2008.12.001

Ferriss, E.D.A., Ewing, R.C., Becker, U., 2010. Simulation of thermodynamic mixing properties of actinide-containing zircon solid solutions. Am. Mineral. 95, 229–241. https://doi.org/10.2138/am.2010.3318

Finch, R.J., Hanchar, J.M., Hoskin, P.W.O., Burns, P.C., 2001. Rare-earth elements in synthetic zircon: Part 2. A single-crystal X-ray study of xenotime substitution. Am. Mineral. 86, 681–689. https://doi.org/10.2138/am-2001-5-608

Förster, H.-J., 2006. Composition and origin of intermediate solid solutions in the system thorite–xenotime–zircon–coffinite. Lithos 88, 35–55. https://doi.org/10.1016/j.lithos.2005.08.003

Fouillac, A.M., Kosakevitch, A., Merceron, T., Meunier, A., Rossi, P., 1987. Comportement des fluides dans l'évolution magmatique puis hydrothermale du granite à Ta, Nb, Li de Beauvoir, d'après la géochimie isotopique de l'oxygène et de l'hydrogène. Géologie Fr. 279–293.

Fuchs, L., Gebert, E., 1958. X-ray studies of synthetic coffinite, thorite and uranothorites. Am. Mineral. J. Earth Planet. Mater. 43, 243–248.

Gagny, C., 1987. Organisation séquentielle évolutive des intrusions successives du granite de Beauvoir dans son caisson : arguments géochimiques. Géologie Fr. 199–208.

Geisler, T., Burakov, B.E., Zirlin, V., Nikolaeva, L., Pöml, P., 2006. A Raman spectroscopic study of high-uranium zircon from the Chernobyl "lava." Eur. J. Mineral. 17, 883–894. https://doi.org/10.1127/0935-1221/2005/0017-0883

Geisler, T., Pidgeon, R.T., Van Bronswijk, W., Kurtz, R., 2002. Transport of uranium, thorium, and lead in metamict zircon under low-temperature hydrothermal conditions. Chem. Geol. 191, 141–154. https://doi.org/10.1016/S0009-2541(02)00153-5

Geisler, T., Schaltegger, U., Tomaschek, F., 2007. Re-equilibration of Zircon in Aqueous Fluids and Melts. Elements 3, 43–50. https://doi.org/10.2113/gselements.3.1.43

Geisler, T., Schleicher, H., 2000. Improved U–Th–total Pb dating of zircons by electron microprobe using a simple new background modeling procedure and Ca as a chemical criterion of fluid-induced U-Th-Pb discordance in zircon. Chem. Geol. 163, 269–285.

Geisler, T., Trachenko, K., Ríos, S., Dove, M.T., Salje, E.K.H., 2003. Impact of self-irradiation damage on the aqueous durability of zircon ($ZrSiO_4$): implications for its suitability as a nuclear waste form. J. Phys. Condens. Matter 15, L597–L605. https://doi.org/10.1088/0953-8984/15/37/L07

Gerstenberger, H., Haase, G., 1997. A highly effective emitter substance for mass spectrometric Pb isotope ratio determinations. Chem. Geol. 136, 309–312. https://doi.org/10.1016/S0009-2541(96)00033-2

Gillespie, J., Klein, B.Z., Moore, J., Müntener, O., Baumgartner, L.P., 2024. A dendritic growth mechanism for producing oscillatory zoning in igneous zircon. Geology. https://doi.org/10.1130/G52641.1

Grolier, J., 1971. Contribution à l'étude géologique des séries crystallophylliennes inverses du massif Central français: la série de la Sioule (Puy de Dôme, Allier). Mém BRGM 64, 163.

Han, J., Hanchar, J.M., Pan, Y., Hollings, P., Chen, H., 2023. Hydrothermal alteration, not metamictization, is the main trigger for modifying zircon in highly evolved granites. Geol. Soc. Am. Bull. https://doi.org/10.1130/B36996.1

Hanchar, J.M., Finch, R.J., Hoskin, P.W., Watson, E.B., Cherniak, D.J., Mariano, A.N., 2001. Rare earth elements in synthetic zircon: Part 1. Synthesis, and rare earth element and phosphorus doping. Am. Mineral. 86, 667–680.

Harlaux, M., Mercadier, J., Bonzi, W.M.-E., Kremer, V., Marignac, C., Cuney, M., 2017. Geochemical Signature of Magmatic-Hydrothermal Fluids Exsolved from the Beauvoir Rare-Metal Granite (Massif Central, France): Insights from LA-ICPMS Analysis of Primary Fluid Inclusions. Geofluids 2017, 1–25. https://doi.org/10.1155/2017/1925817

Hetherington, C.J., Harlov, D.E., 2008. Metasomatic thorite and uraninite inclusions in xenotime and monazite from granitic pegmatites, Hidra anorthosite massif, southwestern Norway: Mechanics and fluid chemistry. Am. Mineral. 93, 806–820. https://doi.org/10.2138/am.2008.2635

Holland, H.D., Gottfried, D., 1955. The effect of nuclear radiation on the structure of zircon. Acta Crystallogr. 8, 291–300. https://doi.org/10.1107/S0365110X55000947

Hoskin, P.W.O., Kinny, P.D., Wyborn, D., Chappell, B.W., 2000. Identifying Accessory Mineral Saturation during Differentiation in Granitoid Magmas: an Integrated Approach. J. Petrol. 41, 1365–1396. https://doi.org/10.1093/petrology/41.9.1365

Hoskin, P.W.O., Schaltegger, U., 2003. The Composition of Zircon and Igneous and Metamorphic Petrogenesis. Rev. Mineral. Geochem. 53, 27–62. https://doi.org/10.2113/0530027

Jaffey, A., Flynn, K., Glendenin, L., Bentley, W. t, Essling, A., 1971. Precision measurement of half-lives and specific activities of U 235 and U 238. Phys. Rev. C 4, 1889.

Kryza, R., Schaltegger, U., Oberc-Dziedzic, T., Pin, C., Ovtcharova, M., 2014. Geochronology of a composite granitoid pluton: a high-precision ID-TIMS U–Pb zircon study of the Variscan Karkonosze Granite (SW Poland). Int. J. Earth Sci. 103, 683–696.

Lafuente, B., Downs, R.T., Yang, H., Stone, N., 2015. The power of databases: the RRUFF project. Highlights Mineral. Crystallogr. T Armbruster R M Danisi Eds Berl. Ger. W Gruyter 1–30.

Large, S.J., Wotzlaw, J.F., Guillong, M., von Quadt, A., Heinrich, C.A., 2020. Resolving the timescales of magmatic and hydrothermal processes associated with porphyry deposit formation using zircon U-Pb petrochronology. Geochronol. Discuss. 2020, 1–39.

Le Roux, L., Glendenin, L., 1963. Half-life of 232Th, in: Proceedings of the National Meeting on Nuclear Energy, Pretoria, South Africa. p. 94.

Leuthold, J., Müntener, O., Baumgartner, L.P., Putlitz, B., Ovtcharova, M., Schaltegger, U., 2012. Time resolved construction of a bimodal laccolith (Torres del Paine, Patagonia). Earth Planet. Sci. Lett. 325–326, 85–92. https://doi.org/10.1016/j.epsl.2012.01.032

Linnen, R.L., Keppler, H., 2002. Melt composition control of Zr/Hf fractionation in magmatic processes. Geochim. Cosmochim. Acta 66, 3293–3301. https://doi.org/10.1016/S0016-7037(02)00924-9

Linnen, R.L., Van Lichtervelde, M., Cerny, P., 2012. Granitic Pegmatites as Sources of Strategic Metals. Elements 8, 275–280. https://doi.org/10.2113/gselements.8.4.275

Liu, X.-H., Li, B., Lai, J.-Q., Jiang, S.-Y., 2022. Multistage in situ fractional crystallization of magma produced a unique rare metal enriched quartz-zinnwaldite-topaz rock. Ore Geol. Rev. 151, 105203. https://doi.org/10.1016/j.oregeorev.2022.105203

London, D., 2018. Ore-forming processes within granitic pegmatites. Ore Geol. Rev. 101, 349–383. https://doi.org/10.1016/j.oregeorev.2018.04.020

London, D., 1992. The application of experimental petrology to the genesis and crystallization of granitic pegmatites. Can. Mineral. 30, 499–540.

López-Moro, F.J., Díez-Montes, A., Timón-Sánchez, S.M., Llorens-González, T., Sánchez-García, T., 2024. Peraluminous Rare Metal Granites in Iberia: Geochemical, Mineralogical, Geothermobarometric, and Petrogenetic Constraints. Minerals 14, 249. https://doi.org/10.3390/min14030249

Lu, T.-Y., He, Z.-Y., Klemd, R., 2023. Different magma differentiation processes of post-onset collision adakitic rocks in the Gangdese Batholith: Evidence from zircon trace elements. Chem. Geol. 620, 121345. https://doi.org/10.1016/j.chemgeo.2023.121345

Ludwig, K.R., 1998. On the Treatment of Concordant Uranium-Lead Ages. Geochim. Cosmochim. Acta 62, 665–676. https://doi.org/10.1016/S0016-7037(98)00059-3

Ludwig, K.R., 1991. ISOPLOT; a plotting and regression program for radiogenic-isotope data; version 2.53. US Geological Survey,.

McKanna, A.J., Schoene, B., Szymanowski, D., 2024. Geochronological and geochemical effects of zircon chemical abrasion: insights from single-crystal stepwise dissolution experiments. Geochronology 6, 1–20. https://doi.org/10.5194/gchron-6-1-2024

McLean, N.M., Bowring, J.F., Bowring, S.A., 2011. An algorithm for U-Pb isotope dilution data reduction and uncertainty propagation. Geochem. Geophys. Geosystems 12, 1–26. https://doi.org/10.1029/2010GC003478

McLean, N.M., Condon, D.J., Schoene, B., Bowring, S.A., 2015. Evaluating Uncertainties in the Calibration of Isotopic Reference Materials and Multi-Element Isotopic Tracers (EARTHTIME Tracer Calibration Part II). Geochem. Cosmochim. Acta 164, 481–501.

Melleton, J., Gloaguen, E., Frei, D., 2015. Rare-Elements (Li-Be-Ta-Sn-Nb) Magmatism in the European Variscan Belt, a Review. Proceedings 2, 807–810.

Merceron, T., Vieillard, P., Fouillac, A.-M., Meunier, A., 1992. Hydrothermal alterations in the Echassières granitic cupola (Massif central, france). Contrib. Mineral. Petrol. 112, 279–292. https://doi.org/10.1007/BF00310461

Mezger, K., Krogstad, E., 1997. Interpretation of discordant U-Pb zircon ages: An evaluation. J. Metamorph. Geol. 15, 127–140.

Michaud, J.A.-S., Gumiaux, C., Pichavant, M., Gloaguen, E., Marcoux, E., 2020. From magmatic to hydrothermal Sn-Li-(Nb-Ta-W) mineralization: The Argemela area (central Portugal). Ore Geol. Rev. 116, 103215. https://doi.org/10.1016/j.oregeorev.2019.103215

Monnier, L., 2018. Utilisation de la signature LA-ICPMS des quartz et des micas pour la reconstruction du fonctionnement d'un système magmatique et hydrothermal polyphasé. Application au complexe Sn-W d'Echassières (Massif Central, France). Université de Toulouse.

Monnier, L., Laurent, O., Salvi, S., Bernard, C., Leisen, M., de Parseval, P., Josse, C., Descamps-Mandine, A., Duan, Z., Gouy, S., 2024. Of zircons and zircons: The tumultuous story of Zr-Hf and REE during cooling of the Evisa peralkaline rare-metal granite (Corsica, France). Press. https://doi.org/10.13140/RG.2.2.28846.73288

Monnier, L., Salvi, S., Jourdan, V., Sall, S., Bailly, L., Melleton, J., Béziat, D., 2020. Contrasting fluid behavior during two styles of greisen alteration leading to distinct wolframite mineralizations: The Echassières district (Massif Central, France). Ore Geol. Rev. 124, 103648. https://doi.org/10.1016/j.oregeorev.2020.103648

Monnier, L., Salvi, S., Melleton, J., Lach, P., Pochon, A., Bailly, L., Béziat, D., De Parseval, P., 2022. Mica trace-element signatures: Highlighting superimposed W-Sn mineralizations and fluid sources. Chem. Geol. 600, 120866. https://doi.org/10.1016/j.chemgeo.2022.120866

Murakami, T., Chakoumakos, B.C., Ewing, R.C., Lumpkin, G.R., Weber, W.J., 1991. Alpha-decay event damage in zircon. Am. Mineral. 76, 1510–1532.

Nasdala, L., Pidgeon, R., Wolf, D., Irmer, G., 1998. Metamictization and U-Pb isotopic discordance in single zircons: a combined Raman microprobe and SHRIMP ion probe study. Mineral. Petrol. 62, 1.

Nasdala, L., Wenzel, M., Vavra, G., Irmer, G., Wenzel, T., Kober, B., 2001. Metamictisation of natural zircon: accumulation versus thermal annealing of radioactivity-induced damage. Contrib. Mineral. Petrol. 141, 125–144. https://doi.org/10.1007/s004100000235

Neves, J.C., Nunes, J.L., Sahama, T.G., 1974. High hafnium members of the zircon-hafnon series from the granite pegmatites of Zambézia, Mozambique. Contrib. Mineral. Petrol. 48, 73–80.

Ohnenstetter, D., Piantone, P., 1988. Géochimie et évolutions des minéraux du groupe des columbo-tantalites et des minéraux du groype du pyrochlore du sondage GPF-1 Echassières (Allier). Doc. BRGM.

Paul, A.N., Spikings, R.A., Chew, D., Daly, J.S., 2019. The effect of intra-crystal uranium zonation on apatite U-Pb thermochronology: A combined ID-TIMS and LA-MC-ICP-MS study. Geochim. Cosmochim. Acta 251, 15–35. https://doi.org/10.1016/j.gca.2019.02.013

Paul, A.N., Spikings, R.A., Gaynor, S.P., 2021. U-Pb ID-TIMS reference ages and initial Pb isotope compositions for Durango and Wilberforce apatites. Chem. Geol. 586, 120604. https://doi.org/10.1016/j.chemgeo.2021.120604

Pérez-Soba, C., Villaseca, C., Orejana, D., Jeffries, T., 2014. Uranium-rich accessory minerals in the peraluminous and perphosphorous Belvís de Monroy pluton (Iberian Variscan belt). Contrib. Mineral. Petrol. 167, 1008. https://doi.org/10.1007/s00410-014-1008-4

Pichavant, M., 2022. Experimental crystallization of the Beauvoir granite as a model for the evolution of Variscan rare metal magmas. J. Petrol. 1–28.

Pichavant, M., Kontak, D.J., Herrera, J.V., Clark, A.H., 1988. The Miocene-Pliocene Macusani Volcanics, SE Peru. Contrib. Mineral. Petrol. 300–324.

Pin, C., 1991. Sr-Nd isotopic study of igneous and metasedimentary enclaves is some hercynian granitoids from the Massif Central, France. In: Didier, J., Barbarin, B. (Eds.), Enclaves and Granite Petrology (Developments in Petrology). Elsevier 13, 33–343.

Popov, D.V., Spikings, R.A., Scaillet, S., O'Sullivan, G., Chew, D., Badenszki, E., Daly, J.S., Razakamanana, T., Davies, J.H.F.L., 2020. Diffusion and fluid interaction in Itrongay pegmatite (Madagascar): Evidence from in situ 40Ar/39Ar dating of gem-quality alkali feldspar and U Pb dating of protogenetic apatite inclusions. Chem. Geol. 556, 119841. https://doi.org/10.1016/j.chemgeo.2020.119841

Raimbault, L., Cuney, M., Azencott, C., Duthou, J.-L., Joron, J.L., 1995. Geochemical evidence for a multistage magmatic genesis of Ta-Sn-Li mineralization in the granite at Beauvoir, French Massif Central. Econ. Geol. 90, 548–576. https://doi.org/10.2113/gsecongeo.90.3.548

Ramakrishnan, S., Gokhale, K., Subbarao, E., 1969. Solid solubility in the system zircon-hafnon. Mater. Res. Bull. 4, 323–327.

René, M., 2014. Composition of coexisting zircon and xenotime in rare-metal granites from the Krušné Hory/Erzgebirge Mts. (Saxothuringian Zone, Bohemian Massif). Mineral. Petrol. 108, 551–569. https://doi.org/10.1007/s00710-013-0318-y

Ribeiro, H.B., Guedes, K.J., Pinheiro, M.V.B., Greulich-Weber, S., Krambrock, K., 2005. About the blue and green colours in natural fluorapatite. Phys. Status Solidi C 2, 720–723. https://doi.org/10.1002/pssc.200460274

Rocher, O., Ballouard, C., Richard, A., Monnier, L., Carr, P.A., Laurent, O., Khebabza, Y., Lecomte, A., Bouden, N., Villeneuve, J., Barré, B., Fullenwarth, P., Leisen, M., Mercadier, J., 2024. Unravelling the magmatic and hydrothermal evolution of rare-metal granites through apatite geochemistry and geochronology: the Variscan Beauvoir granite (French Massif Central). Chem. Geol.

Romer, R.L., Lüders, V., 2006. Direct dating of hydrothermal W mineralization: U–Pb age for hübnerite (MnWO4), Sweet Home Mine, Colorado. Geochim. Cosmochim. Acta 70, 4725–4733.

Romer, R.L., Smeds, S.-A., 1994. Implications of U-Pb ages of columbite-tantalites from granitic pegmatites for the Palaeoproterozoic accretion of 1.90–1.85 Ga magmatic arcs to the Baltic Shield. Precambrian Res. 67, 141–158.

Rossi, Autran, A., Azencott, C., Burnol, L., Cuney, M., Johan, V., Kosakevitch, A., Ohnenstetter, D., Monier, G., Piantone, P., Raimbault, L., Viallefond, L., 1987. Logs pétrographique et géochimique du granite de Beauvoir dans le sondage " Echassières I ". Minéralogie et géochimie comparées. Géologie Fr. 111–135.

Salje, E., Chrosch, J., Ewing, R., 1999. Is "metamictization" of zircon a phase transition? Am. Mineral. 84, 1107–1116.

Scaillet, B., Pichavant, M., Roux, J., 1995. Experimental crystallization of leucogranite magmas. J. Petrol. 36, 663–705.

Schaltegger, U., 2007. Hydrothermal zircon. Elements 3, 51–79.

Schaltegger, U., Ovtcharova, M., Gaynor, S.P., Schoene, B., Wotzlaw, J.-F., Davies, J.F.H.L., Farina, F., Greber, N.D., Szymanowski, D., Chelle-Michou, C., 2021. Long-term repeatability and interlaboratory reproducibility of high-precision ID-TIMS U–Pb geochronology. J. Anal. At. Spectrom. 36, 1466–1477. https://doi.org/10.1039/D1JA00116G

Schaltegger, U., Ovtcharova, M., Schoene, B., 2024. High-precision CA-ID-TIMS U-Pb geochronology of zircon: Materials, methods, and interpretations, in: Methods and Applications of Geochronology. Elsevier, pp. 19–52.

Schmitz, M.D., Schoene, B., 2007. Derivation of isotope ratios, errors, and error correlations for U-Pb geochronology using ^{205} Pb-^{235} U-(^{233} U)-spiked isotope dilution thermal ionization mass spectrometric data. Geochem. Geophys. Geosystems 8, 2006GC001492. https://doi.org/10.1029/2006GC001492

Schoene, B., Schaltegger, U., Brack, P., Latkoczy, C., Stracke, A., Günther, D., 2012. Rates of magma differentiation and emplacement in a ballooning pluton recorded by U–Pb TIMS-TEA, Adamello batholith, Italy. Earth Planet. Sci. Lett. 355–356, 162–173. https://doi.org/10.1016/j.epsl.2012.08.019

Shannon, R.D., 1976. Revised effective ionic radii and systematic studies of interatomic distances in halides and chalcogenides. Found. Crystallogr. 32, 751–767.

Speer, J.A., 1980. Zircon. Mineral. Soc. Am. Rev. Mineral. 5, 67–112.

Speer, J.A., Cooper, B.J., 1982. Crystal structure of synthetic hafnon, HfSiO4, comparison with zircon and the actinide orthosilicates. Am. Mineral. 67, 804–808.

Stacey, J.S., Kramers, J.D., 1975. Approximation of terrestrial lead isotope evolution by a two-stage model. Earth Planet. Sci. Lett. 26, 207–221.

Švecová, E., Čopjaková, R., Losos, Z., Škoda, R., Nasdala, L., Cícha, J., 2016. Multi-stage evolution of xenotime–(Y) from Písek pegmatites, Czech Republic: an electron probe micro-analysis and Raman spectroscopy study. Mineral. Petrol. 110, 747–765. https://doi.org/10.1007/s00710-016-0442-6

Tanabe, K., Hiraishi, J., 1980. Correction of finite slit width effects on Raman line widths. Spectrochim. Acta Part Mol. Spectrosc. 36, 341–344. https://doi.org/10.1016/0584-8539(80)80141-3

Troch, J., Ellis, B.S., Schmitt, A.K., Bouvier, A.-S., Bachmann, O., 2018. The dark side of zircon: textural, age, oxygen isotopic and trace element evidence of fluid saturation in the subvolcanic reservoir of the Island Park-Mount Jackson Rhyolite, Yellowstone (USA). Contrib. Mineral. Petrol. 173, 54. https://doi.org/10.1007/s00410-018-1481-2

Uher, P., Černý, P., 1998. Zircon in Hercynian granitic pegmatites of the western Carpathians, Slovakia. Geol. Carpathica 49, 261–270.

Ushakov, S.V., Gong, W., Yagovkina, M.M., Helean, K.B., Lutze, W., Ewing, R.C., 1999. Solid solutions of Ce, U and Th in zircon. Ceram. Trans. 93, 357–363.

Van Lichtervelde, M., Melcher, F., Wirth, R., 2009. Magmatic vs. hydrothermal origins for zircon associated with tantalum mineralization in the Tanco pegmatite, Manitoba, Canada. Am. Mineral. 94, 439–450. https://doi.org/10.2138/am.2009.2952

Van Lichtervelde, M., Salvi, S., Beziat, D., Linnen, R.L., 2007. Textural Features and Chemical Evolution in Tantalum Oxides: Magmatic Versus Hydrothermal Origins for Ta Mineralization in the Tanco Lower Pegmatite, Manitoba, Canada. Econ. Geol. 102, 257–276. https://doi.org/10.2113/gsecongeo.102.2.257

Wang, X., Griffin, W.L., Chen, J., 2010. Hf contents and Zr/Hf ratios in granitic zircons. Geochem. J. 44, 65–72. https://doi.org/10.2343/geochemj.1.0043

Wark, D.A., Miller, C.F., 1993. Accessory mineral behavior during differentiation of a granite suite: monazite, xenotime and zircon in the Sweetwater Wash pluton, southeastern California, U.S.A. Chem. Geol. 110, 49–67. https://doi.org/10.1016/0009-2541(93)90247-G

Watson, E.B., Wark, D.A., Thomas, J.B., 2006. Crystallization thermometers for zircon and rutile. Contrib. Mineral. Petrol. 151, 413–433. https://doi.org/10.1007/s00410-006-0068-5

Widmann, P., Davies, J.H.F.L., Schaltegger, U., 2019. Calibrating chemical abrasion: Its effects on zircon crystal structure, chemical composition and U Pb age. Chem. Geol. 511, 1–10. https://doi.org/10.1016/j.chemgeo.2019.02.026

Wyllie, P.J., Tuttle, O.F., 1964. Experimental investigation of silicate systems containing two volatile components. Part III. The effect of SO3, P2O5, HCl, and LIéO, in addition to H2O, on the Melting Temperatures of Albite and Granite. Am. J. Sci. 262, 930–939.

Yang, M., Yang, Y.-H., Romer, R.L., Che, X.-D., Wang, R.-C., Wu, F.-Y., Fei, G.-C., Deng, Y., Wu, T., 2023. Characterization of reference materials for in situ U–Pb dating of columbite group minerals by LA-ICP-MS. J. Anal. At. Spectrom. 38, 1816–1829.

Zaraisky, G.P., Aksyuk, A.M., Devyatova, V.N., Udoratina, O.V., Chevychelov, V.Yu., 2008. Zr/Hf ratio as an indicator of fractionation of rare-metal granites by the example of the Kukulbei complex, eastern Transbaikalia. Petrology 16, 710–736. https://doi.org/10.1134/S0869591108070047

Zoheir, B., Lehmann, B., Emam, A., Radwan, A., Zhang, R., Bain, W.M., Steele-MacInnis, M., Nolte, N., 2020. Extreme fractionation and magmatic–hydrothermal transition in the formation of the Abu Dabbab rare-metal granite, Eastern Desert, Egypt. Lithos 352–353, 105329. https://doi.org/10.1016/j.lithos.2019.105329

Figures

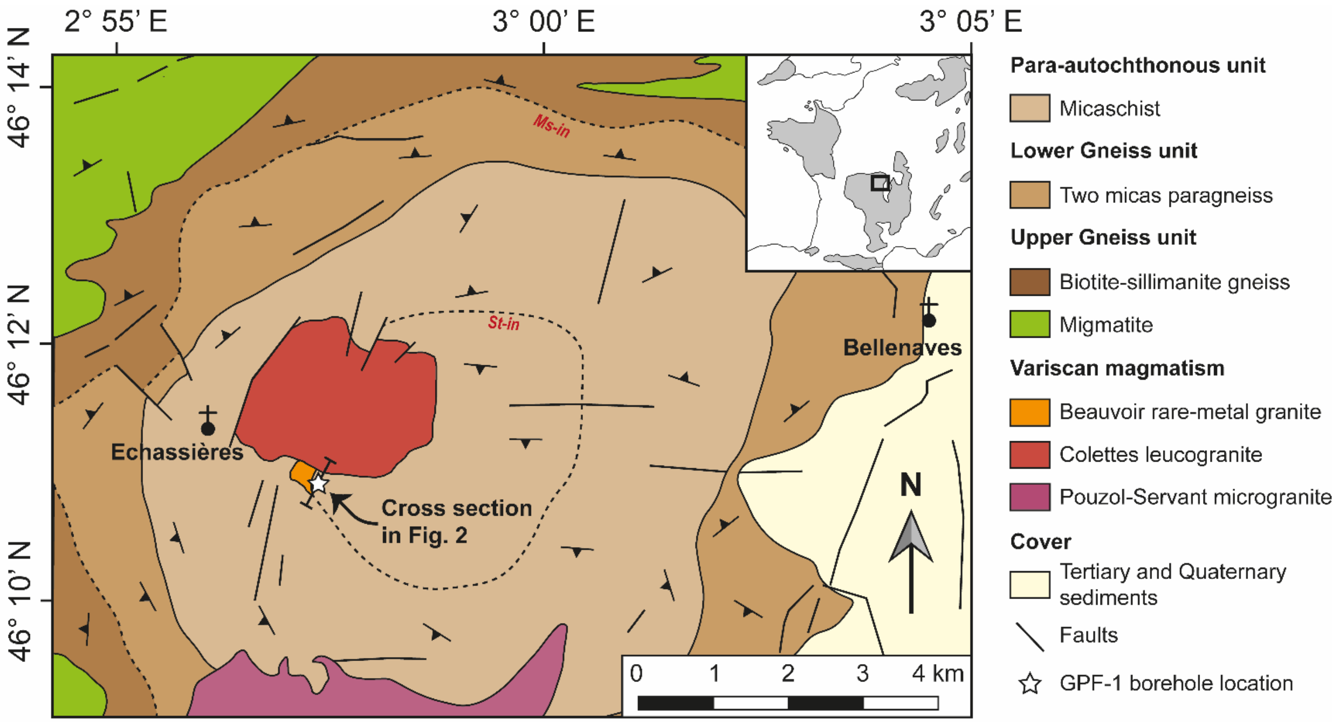

Figure 1. Geological map of the Sioule area, modified from the 1/50 000 geological map of Gannat (BRGM). The top left insert shows the location of the Sioule area within the French Massif Central. Position of the GPF-1 borehole from which the Beauvoir samples have been collected is indicated by the open star. The location of the cross section in

Figure 2 is indicated.

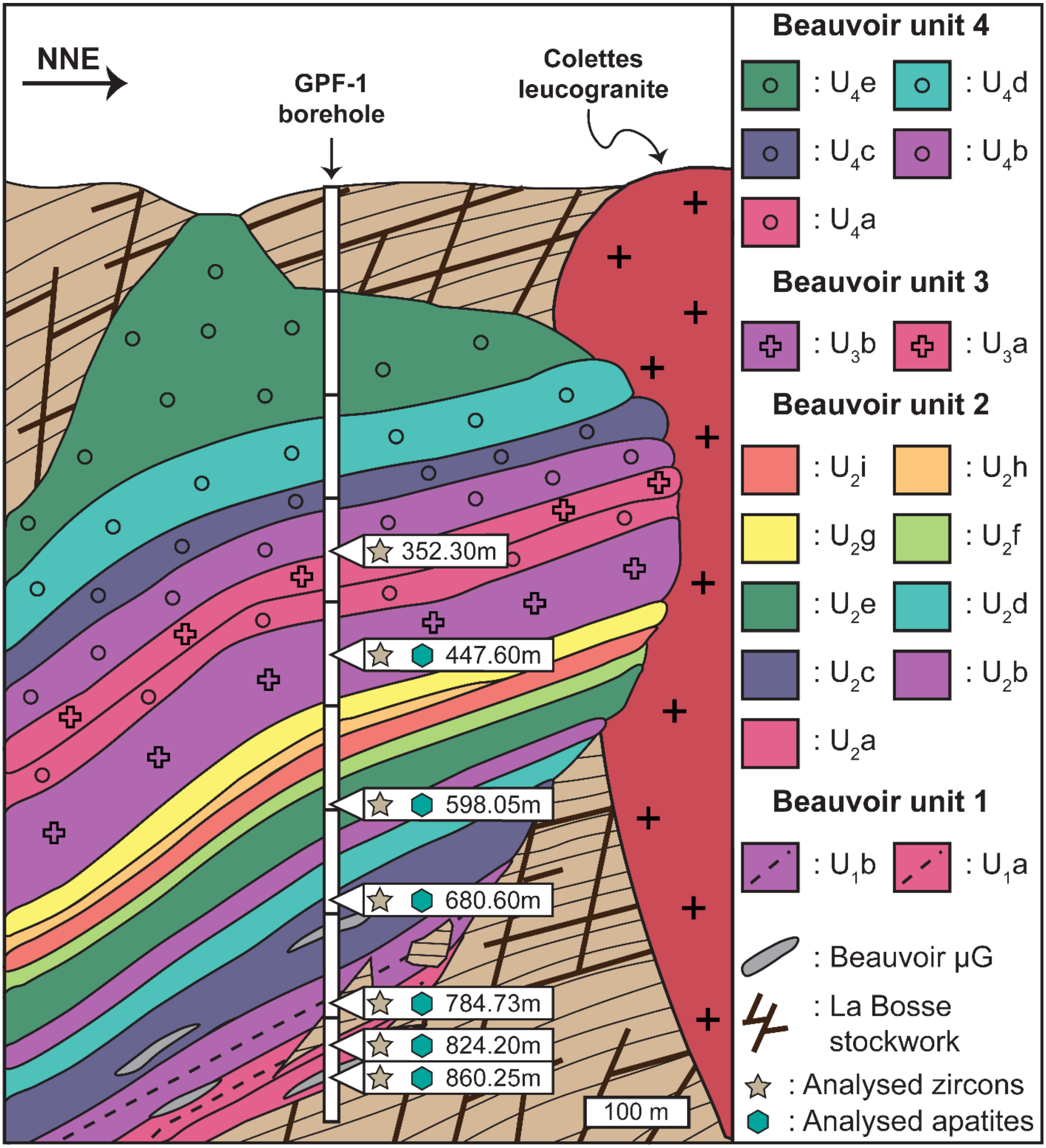

Figure 2. Schematic cross section of the Beauvoir rare-metal granite (localisation indicated in Figure 1). Beauvoir samples from which zircon and apatite grains have been dated are indicated. The location of the eighteen sills (grouped in four main units; U1 to U4) identified by Esteves et al. (2024) based on lepidolite compositional variations throughout the borehole is indicated. The shape of the whole intrusion is from Cuney et al. (1985).

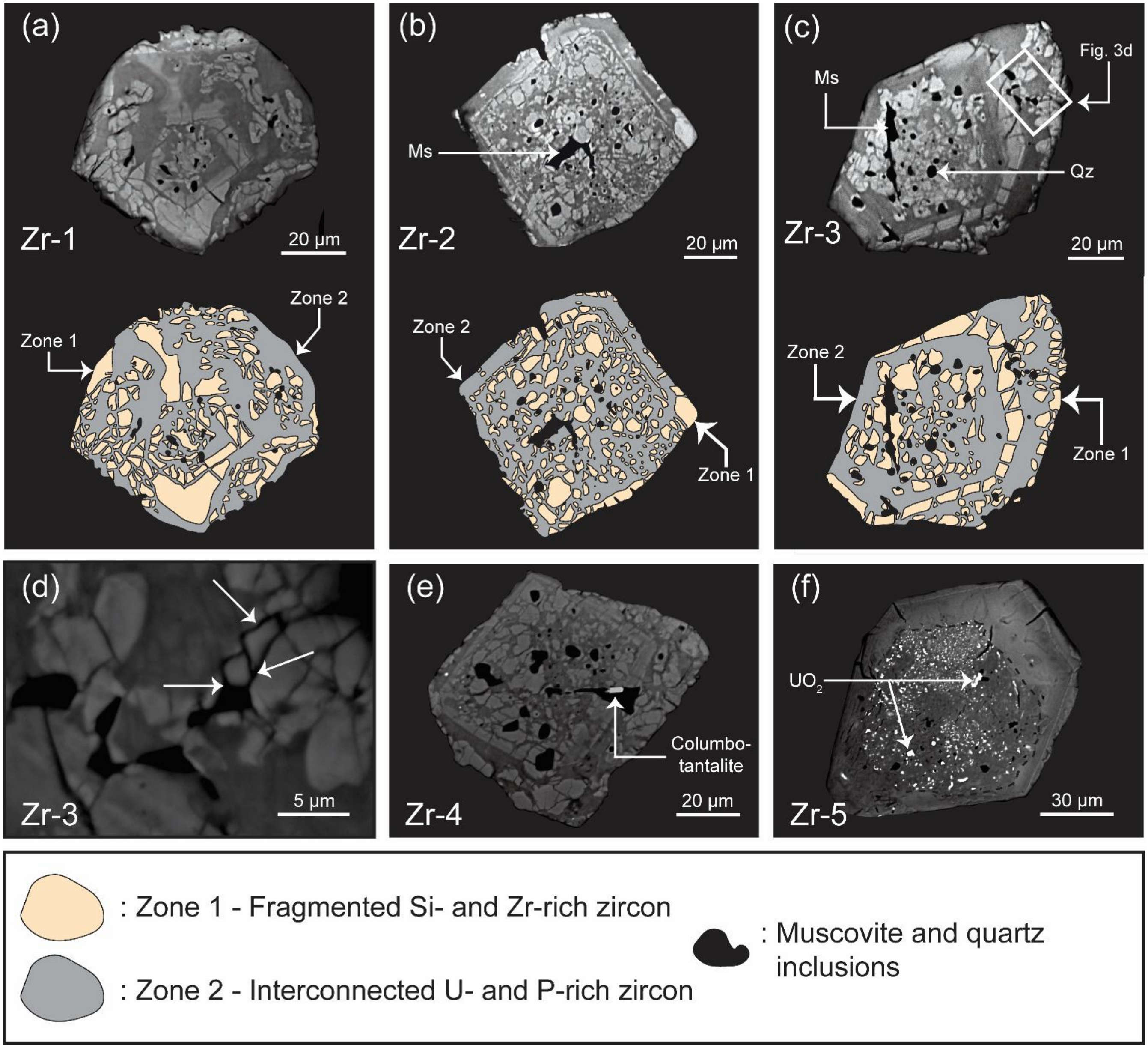

Figure 3. (a-c) Backscattered electron (BSE) images of representative Beauvoir zircon grains with their interpretative scheme. (d) Zoom of the panel (c) presenting the connection between the Al-, Si- and K-rich inclusions and cracks (white arrows). (e) BSE image of Zr-4 where a small columbite-tantalite is included within an Al-, Si- and K-rich inclusion. (f) BSE image of Zr-5 containing a core rich in small UO_2 inclusion. Note the remarkable difference with its homogeneous rim. Zr-1, Zr-2, Zr-3, Zr-4, Zr-5 are the names of the studied individual zircon grains.

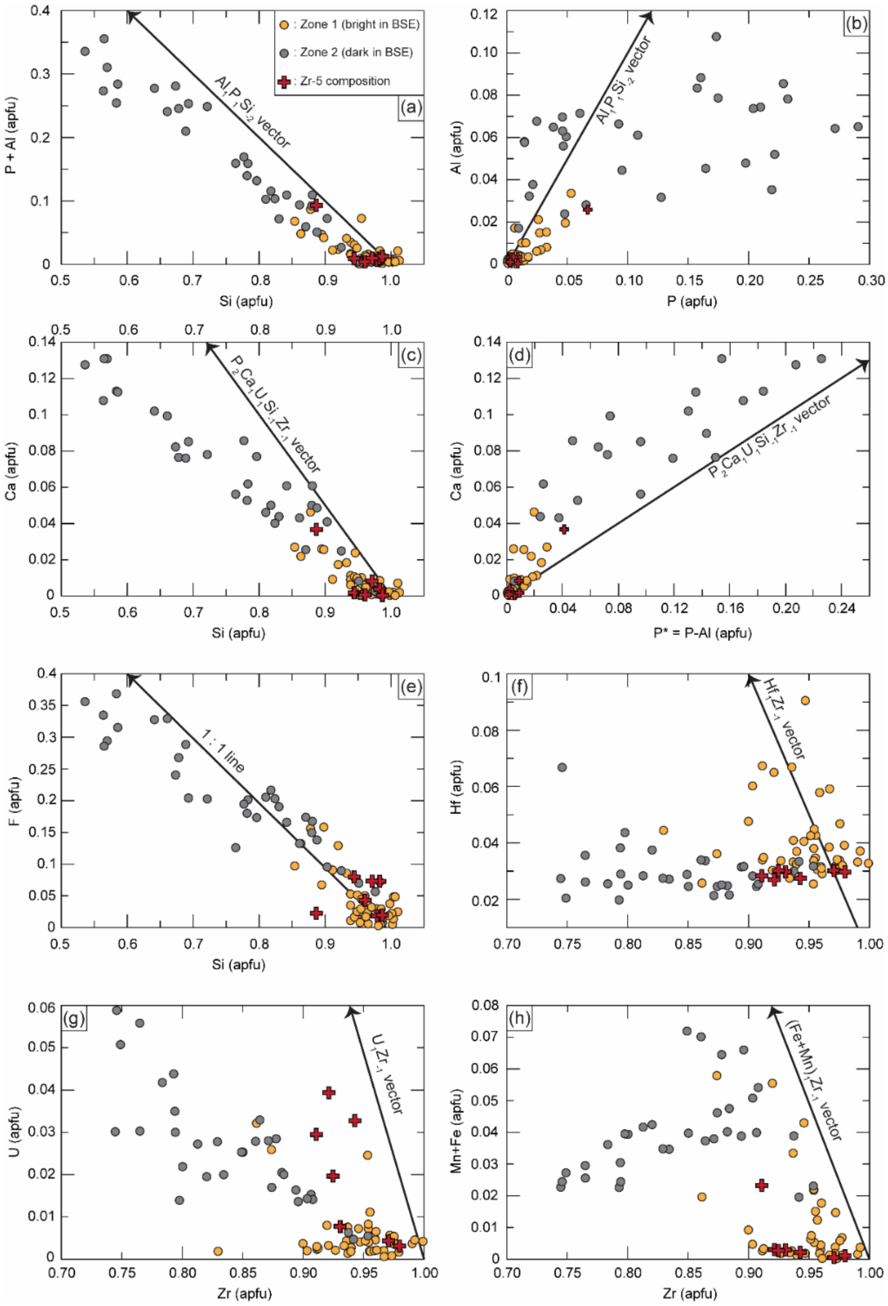

Figure 4. Compositional diagrams in element per formula unit (apfu) for Beauvoir zircon. (a) P + Al vs Si. Note the correlation below the berlinite substitution vector. (b) Al vs P. Note that Zone 2 zircon contains more P than necessary for a berlinite substitution. (c) Ca vs Si. The zircon data form a linear trend below the brabantite substitution vector. d) Ca vs P* where P* = P-Al . P* represents the available P after the berlinite substitution. Note the correlation along the brabantite substitution vector. (e) F vs Si. Note the negative correlation along a 1:1 trend. (f) Hf vs Zr. Note the data do not follow the hafnon substitution vector. (g) U vs Zr. Note the negative correlation below the coffinite substitution vector. (h) Fe + Mn vs Zr. The black arrow corresponds to the theoretical substitution $Zr^{4+} \leftrightarrow 2\ (Fe^{2+} + Mn^{2+})$. In general, note the compositional variations between zone 1 and 2. Also note that except its higher U content, Zr-5 is compositionally similar with Zone 1.

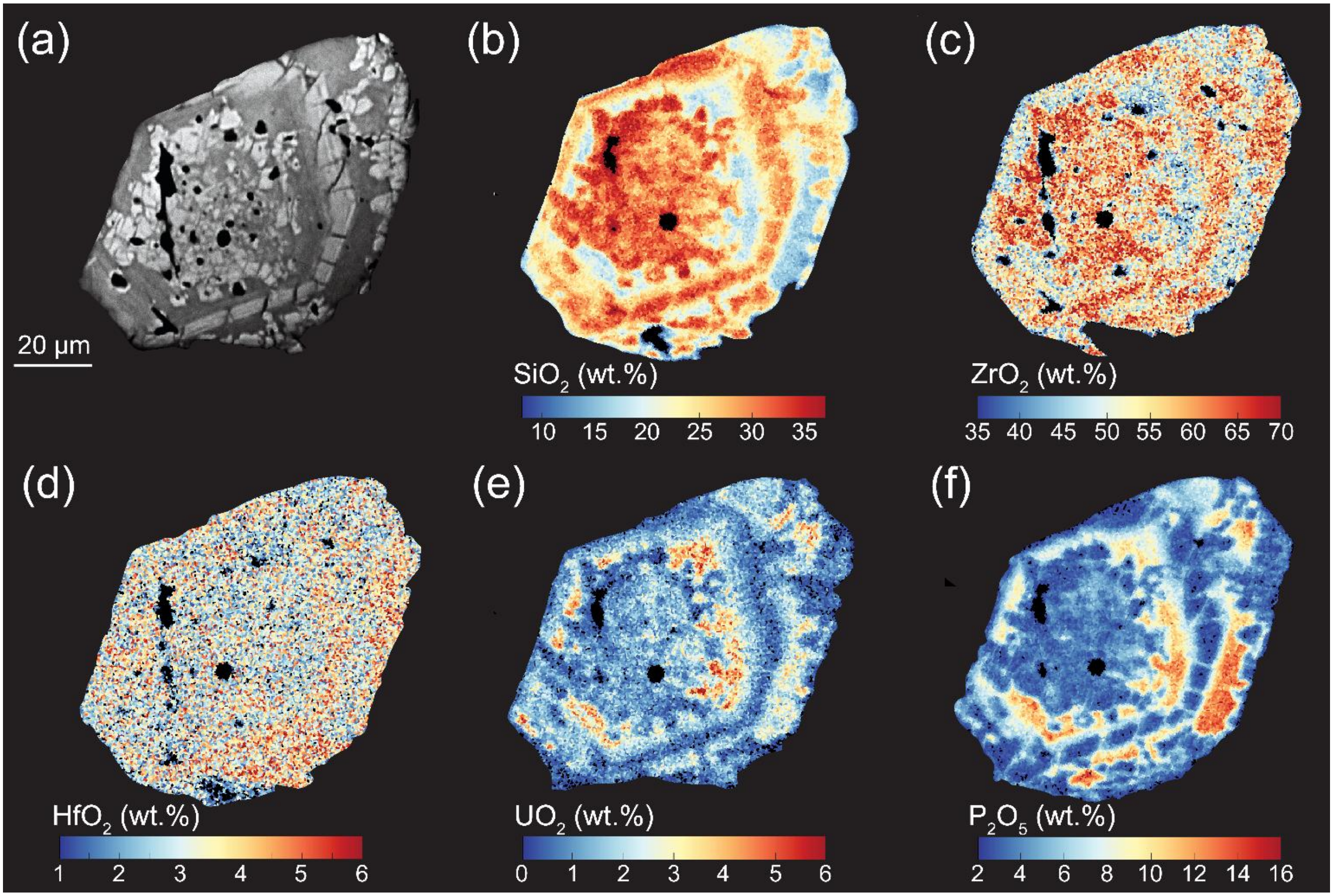

Figure 5. (a) BSE image of Zr-3. (b) SiO_2, (c) ZrO_2, (d) HfO_2, (e) UO_2 and (f) P_2O_5 quantitative chemical maps of the same crystal in (a). Note that the bright domains (Zone 1) in (a) are enriched in Si and Zr whereas the dark domains in (a) are enriched in U and P.

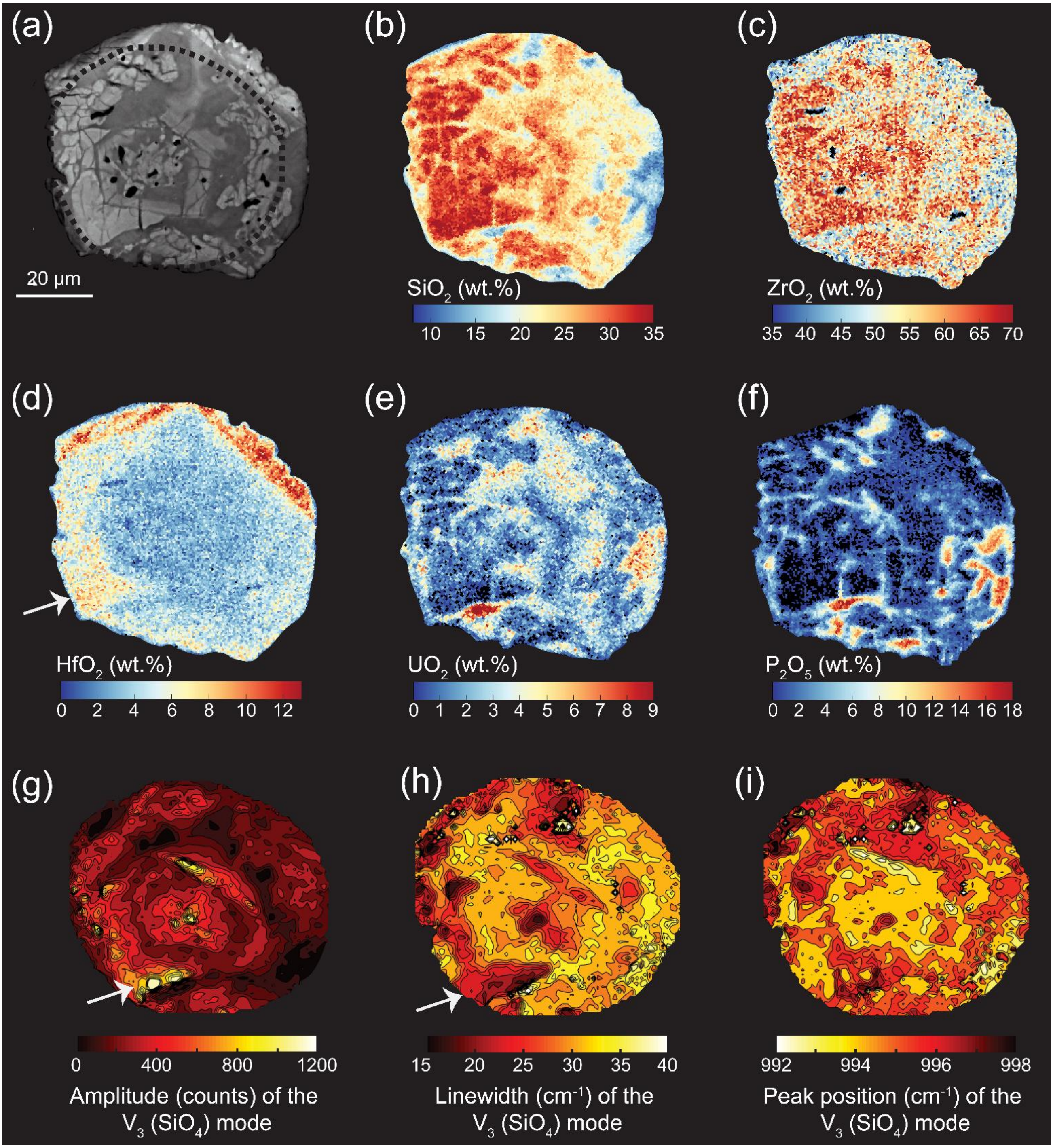

Figure 6. (a) BSE image of Zr-1. (b) SiO_2, (c) ZrO_2, (d) HfO_2, (e) UO_2 and (f) P_2O_5 quantitative chemical maps of the same crystal in (a). (g), (h) and (i) Raman contour maps of the area indicated by the dotted black circle in (a). (g) ν$_3$ (SiO_4) intensity (counts), (h) ν$_3$ (SiO_4) linewidth (cm^{-1}) and (i) ν$_3$ (SiO_4) peak position (cm^{-1}). Note that the Si-, Zr- and Hf-rich area indicated by the white arrow is characterised by a higher ν$_3$ (SiO_4) intensity and a lower ν$_3$ (SiO_4) linewidth.

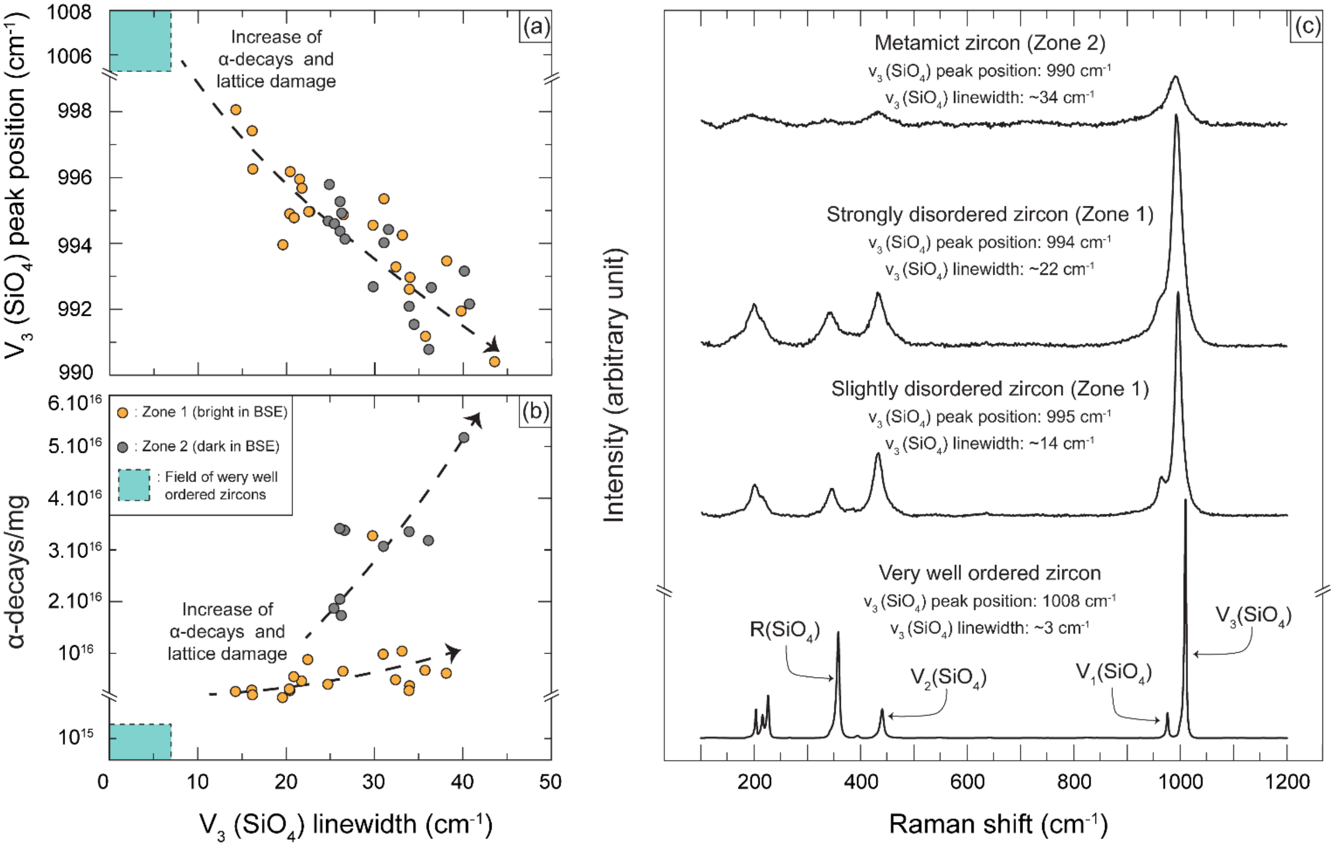

Figure 7. (a) Peak position (cm^{-1}) versus linewidth (cm^{-1}) of the ν$_3$ (SiO$_4$) Zone 1 & 2 Raman band. (b) Calculated α-decays/mg experienced by Zone 1 and 2 versus their ν$_3$ (SiO$_4$) Raman band linewidth (cm^{-1}). Note that in (a) and (b), the y scale is truncated to observe the field of ideal undamaged zircons (from Geisler et al., 2006). (c) Extended zircon Raman spectra from very well ordered to metamict zircon. Very well ordered zircon spectrum is from the RRUFF database (Lafuente et al., 2015) whereas little and strongly disordered spectra correspond to Zone 1 and metamict spectrum corresponds to Zone 2. Note that the lattice ordering degree is strongly related to peak linewidth.

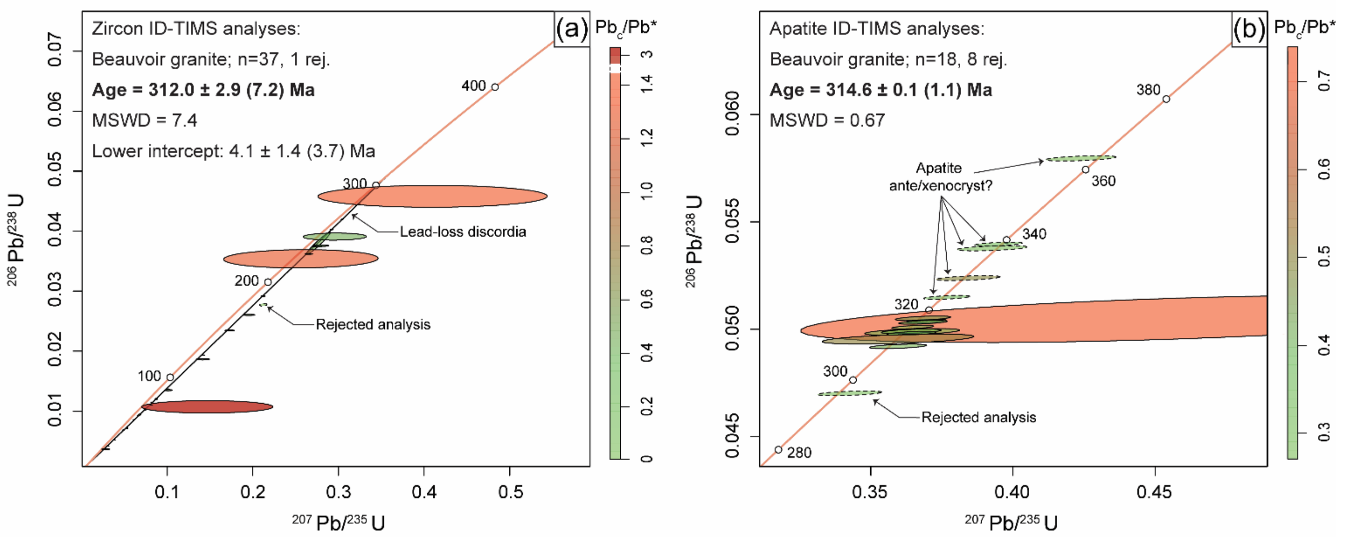

Figure 8. (a) Wetherill diagram showing the zircon analyses straddling a discordia line which intercepts the concordia at 312.0 ± 2.9 (7.2) Ma (2σ). Concordia, Wetherill diagram showing the apatite analyses. Concordant apatite cluster between 309 and 318 Ma give an age at 314.6 ± 0.1 (1.1) Ma (2σ). Ellipses colour represents the common- to radiogenic- lead ratio of each zircon and apatite analysis. The higher this ratio is, the higher the analysis uncertainty is. Complete isotopic results can be found in Table S1.

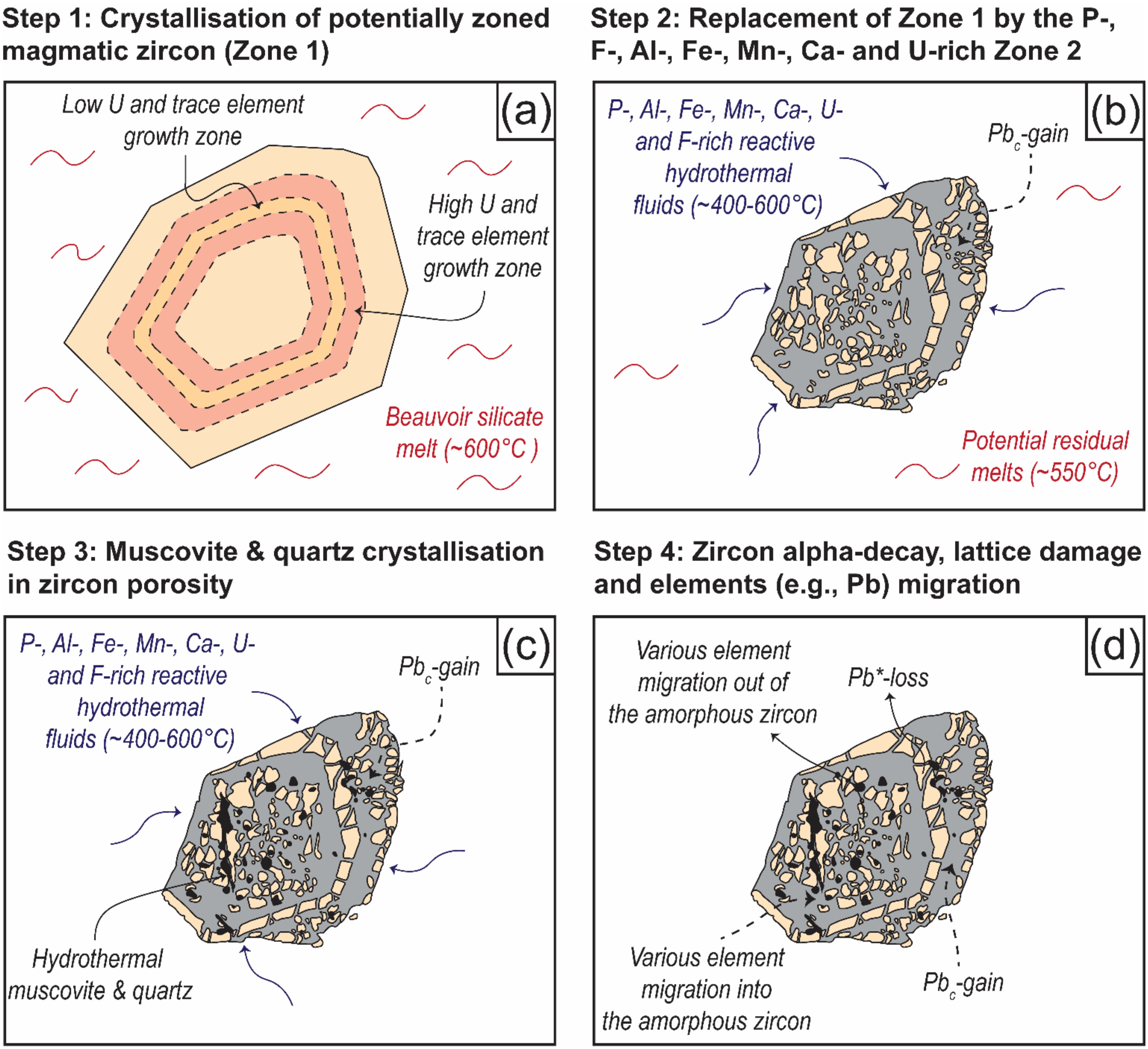

Step 1: Crystallisation of potentially zoned magmatic zircon (Zone 1)

Step 2: Replacement of Zone 1 by the P-, F-, Al-, Fe-, Mn-, Ca- and U-rich Zone 2

Step 3: Muscovite & quartz crystallisation in zircon porosity

Step 4: Zircon alpha-decay, lattice damage and elements (e.g., Pb) migration

Figure 9. Schematic drawing of the formation of Beauvoir zircons. (a) Crystallisation of Zone 1 zircon from the Beauvoir silicate melt. Variations in melt composition through its differentiation formed compositionally distinct growth zones (notably in Hf and U). (b) Partial replacement of Zone 1 by reactive hydrothermal fluids (P-, Al-, Fe-, Mn-, Ca-, U- and F-rich) during the magmatic-hydrothermal transition. The U-rich Zone 1 was preferentially replaced while U-poor Zone 1 was fractured. $\mathrm{Pb_c}$ was likely incorporated the zircon during these replacements. (c) Crystallisation of hydrothermal muscovite and quartz in the zircon voids from reactive fluids of (b). Note that (b) and (c) eventually occurred within the same time period. (d) End of the reactive hydrothermal circulation. Progressive alpha-decay and lattice damage of Beauvoir zircon resulting in metamict state is accompanied by Pb* loss and $\mathrm{Pb_c}$ gain.

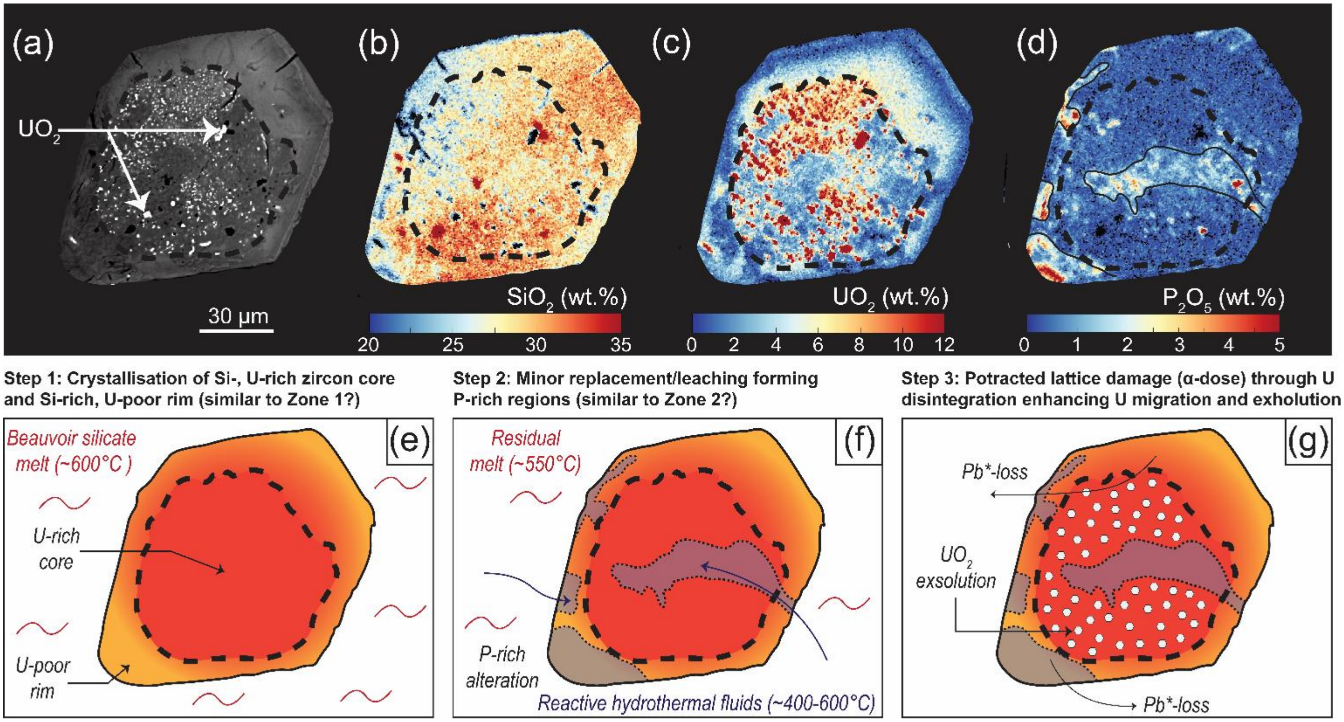

Step 1: Crystallisation of Si-, U-rich zircon core and Si-rich, U-poor rim (similar to Zone 1?)

Step 2: Minor replacement/leaching forming P-rich regions (similar to Zone 2?)

Step 3: Potracted lattice damage (α-dose) through U disintegration enhancing U migration and exholution

Figure 10. (a) BSE image of Zr-5. (b) SiO$_2$, (c) UO$_2$ and (d) P$_2$O$_5$ quantitative chemical maps of the same crystal in (a).. Note the sharp boundary between the crystal core, enriched in uraninite (UO$_2$) micro-inclusions, and the U-rich rim without inclusions, indicated by the dashed circle. Also note the spatial distribution pattern of muscovite and quartz inclusions that are spatially separated from the uraninite inclusions. (e), (f) and (g) Schematic drawing of the formation of Zr-5. (e) Crystallisation of Zr-5 from the Beauvoir silicate melt. Uranium is progressively depleted in the melt leading to a UO$_2$ content decrease from core to rim. (f) Minor replacement and leaching of Zr-5 by reactive residual melt and reactive hydrothermal fluids forming phosphorus-rich domains at the expense of the early-crystallised magmatic Zr-5. (g) Protracted Zr-5 α-dose and lattice damage enhancing UO$_2$ exsolution via U migration through the amorphous zircon.

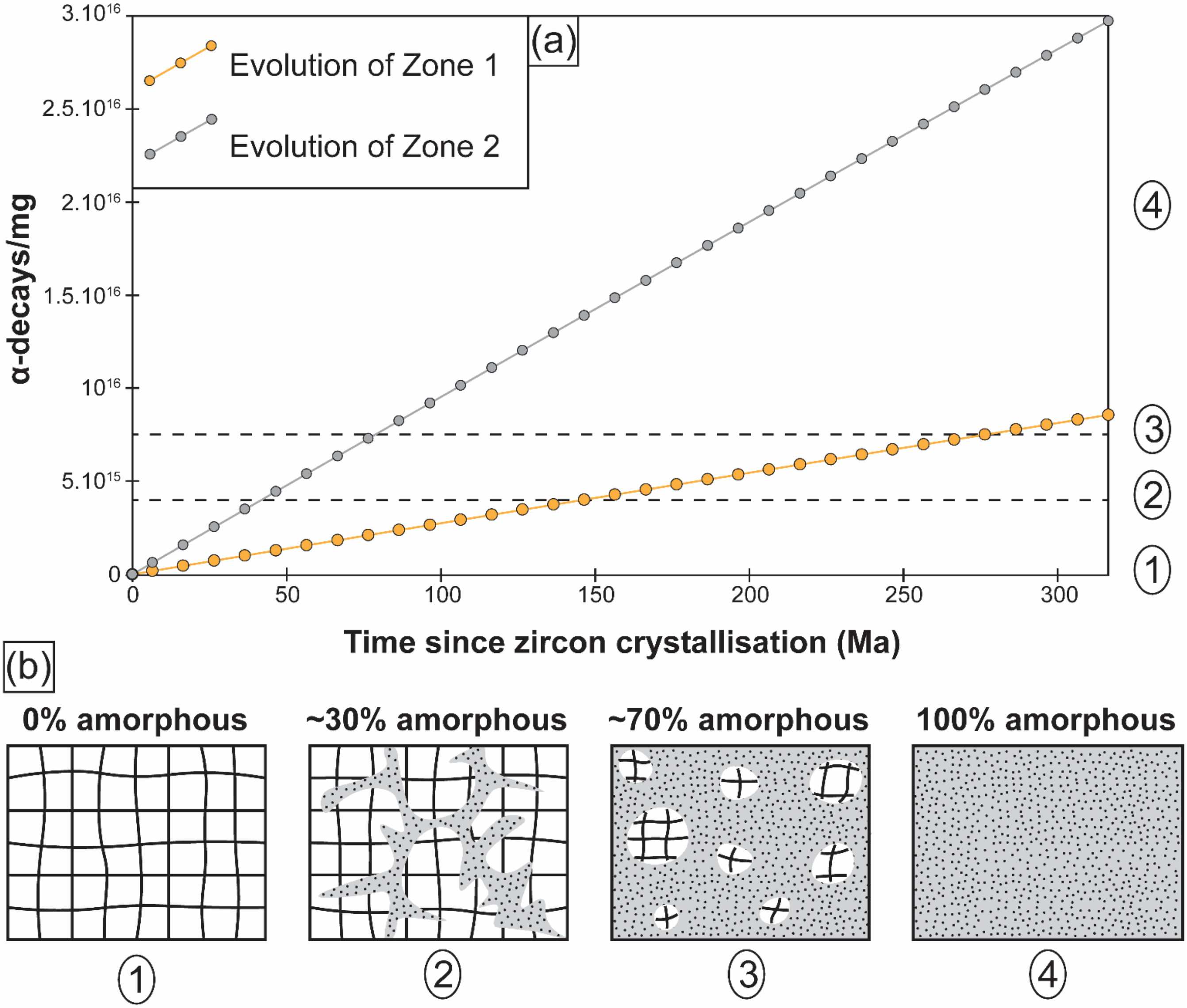

Figure 11. (a) Theoretical evolution of the number of α-decays/mg experienced by Zone 1 and 2 for 314.6 Ma. (b) Schematic representation of the four different steps zircon mesoscopic structure during their protracted lattice damages due to U disintegration, adapted from Murakami et al. (1991). The estimation of amorphous degree for each is from Geisler et al. (2007) and their relations with the number α-dose that experienced zircon is from Nasdala et al. (2001). See text for explanations on the signification of the four different steps.